

Key Points:

- Suspended sand and mud can be distinguished by their different optical and acoustic backscatter signatures
- We define a sediment composition index (SCI) from relative optical and acoustic backscatter and verify it with lab and field measurements
- SCI can be used to estimate the fraction of suspended sand, adding interpretive value to measurements in mixed sediment environments

Supporting Information:

Supporting Information may be found in the online version of this article.

Correspondence to:

S. G. Pearson,
s.g.pearson@tudelft.nl

Citation:

Pearson, S. G., Verney, R., van Prooijen, B. C., Tran, D., Hendriks, E. C. M., Jacquet, M., & Wang, Z. B. (2021). Characterizing the composition of sand and mud suspensions in coastal and estuarine environments using combined optical and acoustic measurements. *Journal of Geophysical Research: Oceans*, 126, e2021JC017354. <https://doi.org/10.1029/2021JC017354>

Received 21 MAR 2021
Accepted 16 JUN 2021

© 2021. The Authors.

This is an open access article under the terms of the [Creative Commons Attribution License](#), which permits use, distribution and reproduction in any medium, provided the original work is properly cited.

Characterizing the Composition of Sand and Mud Suspensions in Coastal and Estuarine Environments Using Combined Optical and Acoustic Measurements

Stuart G. Pearson^{1,2} , Romaric Verney³ , Bram C. van Prooijen¹ , Duc Tran³ , Erik C. M. Hendriks^{1,4} , Matthias Jacquet³, and Zheng Bing Wang^{1,2} 

¹Faculty of Civil Engineering and Geosciences, Delft University of Technology, Delft, The Netherlands, ²Department of Applied Morphodynamics, Deltares, Delft, The Netherlands, ³DYNECO/DHYSED Laboratory, IFREMER, Plouzane, France, ⁴Department of Ecosystems and Sediment Dynamics, Deltares, Delft, The Netherlands

Abstract Quantifying and characterizing suspended sediment is essential to successful monitoring and management of estuaries and coastal environments. To quantify suspended sediment, optical and acoustic backscatter instruments are often used. Optical backscatter systems are more sensitive to mud particles (<63 μm) and flocs, whereas acoustic backscatter systems are more responsive to larger sand grains (>63 μm). It is thus challenging to estimate the relative proportion of sand or mud in environments where both types of sediment are present. The suspended sediment concentration measured by these devices depends on the composition of that sediment, thus it is also difficult to confidently measure concentration with a single instrument when the composition varies and extensive calibration is not possible. The objective of this paper is to develop a methodology for characterizing the relative proportions of sand and mud in mixed sediment suspensions by comparing the response of simultaneous optical and acoustic measurements. We derive a sediment composition index (SCI) that is used to directly predict the relative fraction of sand in suspension. Here, we verify the theoretical response of these optical and acoustic instruments in laboratory experiments and successfully apply this approach to field measurements from Ameland ebb-tidal delta (the Netherlands). Increasing sand content decreases SCI, which was verified in laboratory experiments. A reduction in SCI appears during more energetic conditions when sand resuspension is expected. Conversely, the SCI increases in calmer conditions when sand settles out, leaving behind mud. This approach provides crucial knowledge of suspended sediment composition in mixed sediment environments.

Plain Language Summary Sand and mud particles are the building blocks of our coastlines. Counting and describing sand and mud particles floating through the water is essential to managing coasts. We commonly do this with devices that send out a sound (acoustic) or light (optical) signal into the water. The sensors measure the strength of the signal reflecting back off of any sand and mud particles passing by. Optical instruments are better at “seeing” mud than sand, and acoustic instruments are better at “hearing” sand than mud. If both sand and mud are present, a single instrument will not accurately estimate the total amount of sediment because of these different sensitivities. Instead, we can use both types of instrument together and compare what we “see” with what we “hear.” This comparison allows us to estimate whether there are more sand or mud particles floating through the water. The relationship between “seeing” and “hearing” can be described in a single number, the sediment composition index (SCI). We successfully tested this approach in laboratory experiments and then applied it to a site on the coast of the Netherlands. This approach gives us a new way to understand environments that are both sandy and muddy.

1. Introduction

1.1. Background

Estuaries and coastal seas are characterized by strong morphological and sedimentary gradients, from shallow beaches and intertidal shoals or flats, to deeper foreshore and channel areas or other subtidal features. Furthermore, the sediment composition at a given site may vary widely in both particle size and mineralogy (Flemming & Ziegler, 1995; Son et al., 2011; Winkelmolen & Veenstra, 1974). The size and material

properties of mud (aka “fines” or “fine sediment”) and sand are different: sand particles are individual quasi-spherical grains (with typical density $\rho_s = 2,650 \text{ kg/m}^3$ for quartz particles), between 63 and 2,000 μm in diameter, d . Muddy sediments, especially clay particles ($d < 2 \mu\text{m}$), have the ability to flocculate and often bond with organic matter. The resulting flocs vary widely in diameter (from 10 to 1,000 μm) and have relatively low densities ($\rho_{floc} = O(1,100 - 2,000 \text{ kg/m}^3)$) with irregular shapes and lower settling velocities than sand (Chapalain et al., 2019; Dankers & Winterwerp, 2007; Eisma, 1993; Fugate & Friedrichs, 2002; P. S. Hill et al., 2000; Khelifa & Hill, 2006; Manning et al., 2006; Many et al., 2019; McCave, 1984; Milligan & Hill, 1998). The spatial distribution of these different types of sediment is a function of morphology, supply, and hydrodynamic conditions.

Due to episodic (storms and floods) and persistent (tides) hydrometeorological forcing and human influences, estuarine and coastal sediment are highly dynamic. Bed sediments are mobilized and transported, through bed load (rolling, sliding, and saltating near the surface of the seabed) or suspended load (held aloft in the water column by turbulence). In this paper, we focus on transport in suspension, dealing with mud ($d < 63 \mu\text{m}$) and very fine to medium sand $d = 63\text{--}500 \mu\text{m}$, the latter being found in suspension (relatively close to the bed) during energetic conditions. Depending on local and remote bed composition and hydrodynamic forcing, the concentration, characteristics, and fluxes of suspended particulate matter (SPM) will drastically change.

The morphological changes resulting from these fluxes may threaten or enhance coastal infrastructure and ecosystems. Quantifying these sediment fluxes is critical for sustainable coastal management (Hanley et al., 2014; Hendriks et al., 2020; Mulder et al., 2011). Measurements of these fluxes can be used to derive sediment budgets (Wang et al., 2018), better understand the physical processes underlying sediment transport (White, 1998), and quantify sediment pathways and connectivity (Pearson et al., 2020). They also allow us to calibrate and improve numerical sediment transport models (Amoudry & Souza, 2011; Roelvink & Reniers, 2012). Of critical importance is not just quantifying total sediment fluxes but also sediment fluxes as a function of particle size. For example, overestimating sand concentration could lead to underestimates of an estuary's ability to import sediment and evolve in equilibrium with accelerating sea level rise (e.g., Lodder et al., 2019).

The main challenge faced in understanding coastal sediment dynamics and quantifying associated fluxes is to make continuous observations of total (sand and mud) suspended sediment and their related mass concentration (SSC). Continuous in situ measurements are possible with acoustic or optical instruments (Fettweis et al., 2019). Optical backscatter (OBS) sensors have been used successfully to measure suspended sediment in a wide range of environments, from estuaries and embayments (Bass et al., 2002, 2007; Fettweis et al., 2019; Fugate & Friedrichs, 2002; Green et al., 2000; Li et al., 2018; Lin et al., 2020; Lunven & Gentien, 2000) to mud flats and salt marshes (Guo et al., 2018; Voulgaris & Meyers, 2004) to sandy beaches (Aagaard et al., 2002; J. P. Downing et al., 1981). Acoustic backscatter sensors have also been successfully used to measure suspended sediment in many different coastal and estuarine settings (Bass et al., 2007; Chanson et al., 2008; Fugate & Friedrichs, 2002; Green et al., 2000; Hoitink & Hoekstra, 2005; Li et al., 2018; Lin et al., 2020; Thorne et al., 1993; Voulgaris & Meyers, 2004) and beyond (Hawley, 2004; D. C. Hill et al., 2003).

The measurement capabilities of optical and acoustic backscatter instruments are inextricably tied to the material properties of the sediment they observe. Each type of instrument responds with different sensitivity to muddy or sandy sediment because of a dependence on particle size and density. Hence, in practice, empirical calibration models for optical or acoustic sensors are built via regression against laboratory or in situ samples, the latter providing reference gravimetric concentrations (Fettweis et al., 2019; J. Gray & Elliott, 2009). Once the calibration for a given instrument has been developed, the calibrated relationship can be applied to the recorded signal from the field (e.g., voltage, nephelometric turbidity units [NTU], counts, or signal-to-noise ratio [SNR]) and translated into a time series of mass concentration. This concentration can then be interpreted in light of other measurements such as velocity.

However, these calibration models are representative of a given condition (e.g., calm, moderate tidal flows with SPM dominated by mud) and may not be well adapted for observing a succession of low- and high-energy conditions when the SPM sand and mud content (f_{sand} and f_{mud}) can vary strongly in time (Bass et al., 2007). The most appropriate methodology would require sampling and recalibrating sensors as fast as

SPM composition changes, but this is neither easily predictable nor realistic. A library of population-adapted calibration models could be built following Green and Boon (1993), but knowledge about SPM composition dynamics is a prerequisite for their application.

In this paper, we develop an original sediment composition index (SCI) derived from optical and acoustic measurements to quantitatively and dynamically evaluate the relative fraction of sand or mud in suspension. The concept is first validated using laboratory measurements, and then applied to field measurements. The SCI index provides researchers with a way to more accurately quantify SSC, especially during high-energy events when calibration with physical samples is not possible.

1.2. Optical Backscatter Measurements

OBS sensors are widely used to indirectly measure suspended sediment concentration. Near-infrared light (typical wavelength $\lambda = 0.780\text{--}0.865\ \mu\text{m}$) is emitted from the instrument, backscattered by suspended particles, and then recorded by photoreceptors. In a Mie scattering regime, backscatter is strongest when the light wavelength and particle size are similar, so *OBS* are more sensitive to mud particles $O(1\ \mu\text{m})$ than sand particles $O(100\ \mu\text{m})$ (Conner & De Visser, 1992; Green & Boon, 1993; Voulgaris & Meyers, 2004). According to Sutherland et al. (2000), the photon flux received by the sensor is given as

$$F = VNE \frac{\pi d^2}{4} Q_s \quad (1)$$

where F is photon flux (W), V is scattering volume (cm^3), N is the number concentration of scatters (cm^{-3}), E emitted irradiance (W/cm^2), d is the particle diameter (μm), Q_s the (back)scattering efficiency of the particles. Relating the number concentration to the mass concentration *SSC* (mg/L), this relationship can be modified as follows (Sutherland et al., 2000):

$$F = \frac{3}{2} \frac{V(SSC)E}{\rho_s d} Q_s \quad (2)$$

where ρ_s is the particle (dry) density (kg/m^3). This flux is then translated to a voltage output by the sensor.

Equation 2 can then be reworked as

$$OBS = \alpha_{OBS} \frac{Q_s}{\rho_s d} SSC \quad (3)$$

where *OBS* is the optical backscatter signal (V) and α_{OBS} is approximated as a constant for the range of *SSC* investigated.

Due to the dependency on $1/(\rho_s d)$, for the same concentration of sediment, the flux observed for $200\ \mu\text{m}$ sand ($\rho_s \approx 2,600\ \text{kg}/\text{m}^3$) will be 10 times smaller than for muddy flocs of the same size ($\rho_{floc} \approx 1,100\ \text{kg}/\text{m}^3$), and even smaller in presence of microflocs. However, this sensitivity to size may be as low as a factor of 2 when intercomparing floc particles with a continuous size distribution from microflocs to macroflocs, rather than the sandy and muddy end members considered in this study (Boss, Slade, & Hill, 2009; Boss, Slade, Behrenfeld, et al., 2009; P. S. Hill et al., 2011).

1.3. Acoustic Backscatter Measurements

Analogously to *OBS* devices, an acoustic signal is emitted and backscattered by particles in suspension, then recorded by transducers. The estimation of *SSC* from acoustic measurements depends on the properties of sediment in suspension. For well-characterized particles (e.g., a well-sorted sand population) and electronically/acoustically calibrated sensors, backscattering models and representative diameters can be used to evaluate *SSC* from the theory (Thorne & Hanes, 2002). Otherwise, similarly to optical sensors, the acoustic response can be calibrated against samples from field or laboratory experiments, with similar limitations regarding calibration representativity.

Acoustic devices typically used in coastal sediment studies can loosely be grouped into (a) single-frequency acoustic Doppler velocimeters (ADV) which measure at a single point; (b) single-frequency acoustic Doppler current profilers (ADCP) which measure over multiple points in the water column; and (c) multifrequency acoustic backscatter devices. Only the latter is specifically designed to measure suspended sediment concentration; ADCPs and ADVs were originally intended to measure velocity, but their operating principles mean that inferring sediment concentration from acoustic backscatter is a useful side benefit. In this study, we mainly consider acoustic backscatter from ADVs, which are widely used to measure suspended sediment concentrations (Fugate & Friedrichs, 2002; Lin et al., 2020; Öztürk, 2017).

We can mathematically describe acoustic backscatter using the sonar equation, which balances the difference between energy emitted and received by the sensor with energy lost on the return trip of an acoustic pulse (Hoitink & Hoekstra, 2005). The sonar equation is presented here in form similar to (Chmiel et al., 2018; Hoitink & Hoekstra, 2005; Salehi & Strom, 2011)

$$SNR = C - \underbrace{20 \log_{10}(\psi R^2)}_{\text{Spherical Spreading}} - \underbrace{\int_0^R (\alpha_w(r) + \alpha_s(r)) dr}_{\text{Attenuation}} + BI \quad (4)$$

SNR (dB) is the signal-to-noise ratio recorded directly by the ADV, which indicates the intensity of acoustic backscatter. C (dB) is a constant including instrument-related and geometrical terms. The spherical spreading term ($20 \log_{10}(\psi R^2)$) is a function of R (m), the one-way distance that the acoustic pulse travels from the transmitter to the measurement volume. The attenuation of the acoustic pulse can be decomposed into absorption by the water α_w (dB/m) and attenuation by sediment α_s (dB/m), integrated over the travel distance. BI is the volume backscatter strength (dB) and is a function of SSC and particle characteristics:

$$BI = 10 \log_{10} \left(\frac{SSC \bar{\sigma}}{\rho_s \bar{V}_s} \right) \quad (5)$$

where $\bar{\sigma}$ is the mean backscattering cross section (m^2), ρ_s is the dry particle density (kg/m^3), and \bar{V}_s is the scattering volume (m^3).

The attenuation terms (α_s and α_w) are higher at larger concentrations and greater distances (Thorne et al., 1993) but can be neglected below 1,000 mg/L (Chmiel et al., 2018) and $O(10$ cm) from the sensor (Pomázi & Baranya, 2020). In this study, we thus neglect attenuation, given the small distance between source and measuring volume (15 cm) and low concentrations expected at our study site in Ameland ($<1,000$ mg/L). All terms except BI can be reorganized and set in a global constant C' [dB]. Equation 5 then becomes

$$SNR = 10 \log_{10}(SSC) + 10 \log_{10} \left(\frac{\bar{\sigma}}{\rho_s \bar{V}_s} \right) + C' \quad (6)$$

Equation 6 can be further simplified as

$$SNR = 10 \log_{10}(SSC) + b' + c' \quad (7)$$

where c' is a constant depending on instrument characteristics and b' is a variable depending on suspended particle properties (e.g., size, shape, density, and elasticity). The log linear relation between SNR and SSC is only valid for concentrations less than 1,000 mg/L (Chmiel et al., 2018; Salehi & Strom, 2011); beyond this threshold, particle absorption losses reduce the recorded backscattering signal.

The interaction between an acoustic pulse and particles (scattering) is optimal for coarser individual (unfloculated) particles, with a dependency on the acoustic frequency such as $kd/2 \approx 1$ (or $< d$) where k is the wave number ($2\pi/\lambda$, and λ is the wavelength) and d the diameter of the particle (Salehi & Strom, 2011). Hence, for a 1 MHz acoustic signal, the optimal backscattering size (diameter) is around 480 μm , while for a 6 MHz signal, the optimal size is around 80 μm . Floculated particles are characterized by lower backscattering efficiency (1–2 order of magnitude lower) (Thorne & Hurther, 2014). Acoustic instruments are

thus more sensitive to fine to coarse sands than flocculated mud particles (Salehi & Strom, 2011): for similar concentrations, the SNR will be stronger for sand than for mud.

1.4. Combining Optical and Acoustic Measurements: Toward the SCI

In coastal and estuarine environments where suspended particles are often characterized by a mixture of mud (including flocs) and sand particles, SSC measurements relying on a single technique (optical or acoustic) are ambiguous with respect to sediment composition. This can lead to misestimates of particle size and concentration (Thorne et al., 2021) and limits the interpretability and representativeness of the recorded signal. The objective of the present paper is to combine the use of optical and acoustic backscatter sensors to estimate the relative fraction of sand in suspension.

Bass et al. (2007) note that although optical and acoustic backscatter systems are routinely used together, few studies have taken advantage of using them together to estimate suspended sediment composition in mixed environments. There is a salient difference in the response of optical and acoustic instruments to changes in suspended particle size (Ha et al., 2009), which may be exploited to resolve ambiguities.

In some cases, it has been assumed that optical or acoustic instruments only observe a single class of sediment. Bass et al. (2002) disregard locally resuspended sand in their OBS measurements of mud. In studies of tidal channels flanked by intertidal mud flats, both Green et al. (2000) and van de Kreeke and Hibma (2005) assumed that optical sensors detected only silt, while acoustic sensors detected only sand. The interpretation of a single instrument depends on the assumptions behind its calibration (e.g., an OBS calibrated to sandy sediment will overestimate total SSC when mud is also present). However, instead of ignoring the presence of sand in optical measurements or the presence of mud in acoustic measurements, paired instruments can more beneficially be used concurrently and compared (Conner & De Visser, 1992; Green & Boon, 1993; Hawley, 2004). In this study, we take advantage of these paired instruments to derive a SCI that quantitatively discriminates the presence of suspended sand from mud.

This relative optical-acoustic backscatter response can be analyzed by combining Equations 3 and 7 to obtain:

$$SNR = 10 \log_{10}(OBS) + b_{particle} + c_{instr} \quad (8)$$

where $b_{particle}$ is a variable parameter function of SPM characteristics and c_{instr} is a global (optical/acoustic) instrument-related constant. In our study, as instruments were not calibrated, $b_{particle} + c_{instr}$ are considered as a single constant, the SCI. SCI is therefore dependent on the characteristics of the sediment particles being measured and of the instruments being used. Equation 8 can be rearranged to present SCI:

$$SCI = 10 \log_{10}(OBS) - SNR \quad (9)$$

Considering the high sensitivity of the acoustic sensor to sand and of the optical sensor to mud, SCI is relatively smaller when suspended sand particles dominate and relatively larger when mud dominates suspensions. SCI can thus be used as an indicator of sand or mud dominance.

2. Methods

Laboratory measurements were used as a proof of concept for the SCI and to quantify the relationship between SCI and the fraction of sand in suspension (f_{sand}). The fraction of mud in suspension can also be directly calculated via $f_{mud} = 100\% - f_{sand}$. We then analyze in situ measurements to demonstrate the added value of SCI for investigating the dynamics of mixed sediment environments. We compared optical/acoustic signals measured on Ameland ebb-tidal delta in the Netherlands during a 40-day period featuring storms and calm conditions. From these signals, we calculated SCI and f_{sand} and put them into context with other simultaneous measurements (tidal stage) and derived parameters (bed shear stress due to waves and currents). By interpreting these measurements, we can test whether SCI is a valid and useful indicator of relative suspended sand or mud dominance in estuarine environments.

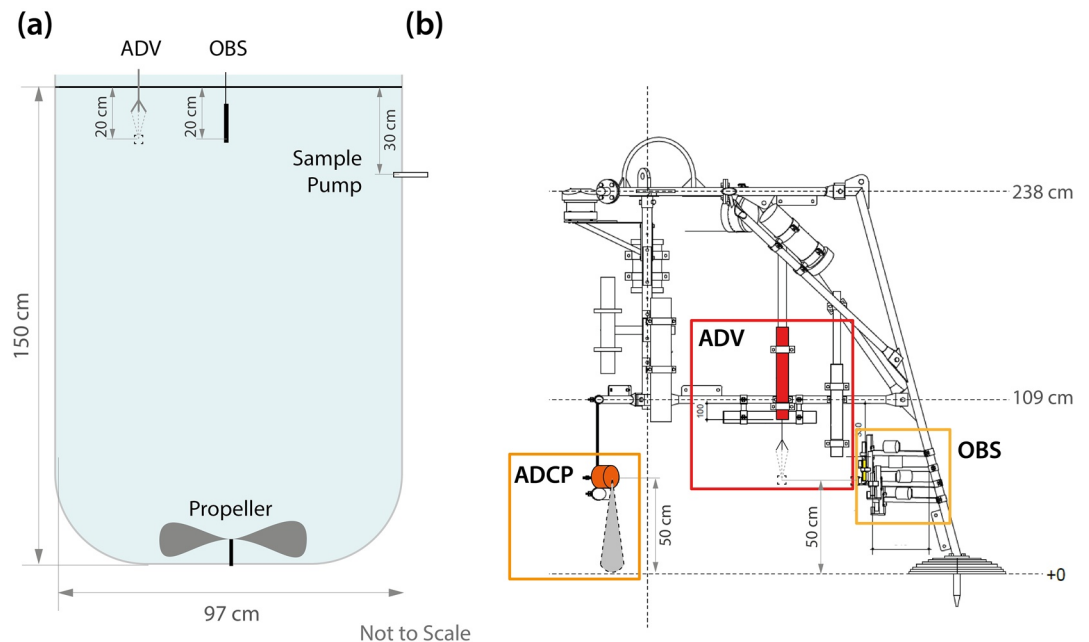


Figure 1. Overview of the DEXMES tank used in the laboratory experiments. (a) Schematic of instrument setup. During the experiments, the tank contained an acoustic Doppler velocimeter (ADV) and an Optical Backscatter (OBS) sensor mounted just below the surface. An external pump was connected to the tank to extract suspended sediment samples. (b) Frame used to conduct field measurements (Amelander Zeegat [Ameland Inlet] Frame #4 [AZG F4]), featuring ADVs, OBSs, and an downward-facing acoustic Doppler current profiler (ADCP) sensors. The ADV and OBS measured sample volumes 50 cm above the base of the frame, and the ADCP measured a 50-cm profile between the instrument and the bed. DEXMES, Dispositif EXPérimental de quantification des Matières En Suspension.

2.1. Laboratory Experiments

We used the DEXMES (Dispositif EXPérimental de quantification des Matières En Suspension) tank for our experiments. DEXMES is operated by Ifremer and managed together with Géosciences Océan, Géosciences Rennes and SHOM (French Hydrographic Service). The glass-walled tank has a volume of approximately 1 m³ and internal diameter of 0.97 m (Figure 1) and was filled with fresh water.

Two sets of similar experiments were conducted to evaluate SCI at various total sediment concentration ranges and sand/mud contents. In Experiment 1, pure bentonite ($d_{50} = 17 \mu\text{m}$) and two classes of well-sorted pure quartz sand ($\rho_s = 2,650 \text{ kg/m}^3$) with median grain sizes $d_{50} = 100$ and $220 \mu\text{m}$ were used. Conversely, Experiment 2 used estuarine mud ($d_{50} = 15 \mu\text{m}$) instead of bentonite, and the same sources of sand but without further sieving ($d_{50} = 93$ and $210 \mu\text{m}$). The estuarine mud contained organic matter, but this was not quantified. For simplicity, we hereafter refer to $d_{50} \approx 100 \mu\text{m}$ and $d_{50} \approx 200 \mu\text{m}$ sand for both experiments. In the context of these experiments, “mud” refers to bentonite and estuarine mud ($d_{50} < 63 \mu\text{m}$), while “coarse sediment” or “sand” refers to both size classes of sand ($d_{50} > 63 \mu\text{m}$).

Five sediment composition conditions were investigated for both 100 and 200 μm sand in Experiment 1: pure bentonite, pure sand, and three intermediate mixtures: 25%, 50%, and 75% sand content (f_{sand}). For each condition, six total concentrations were tested stepwise from 15 to 200 mg/L (see Appendix A). In Experiment 2, the (estuarine mud) concentration was held constant at approximately 130 mg/L and sand concentration (100 or 200 μm) incrementally varied between 0 and 1,460 mg/L (see Appendix A), in order to approximate an estuarine environment with a sandy local bed composition and steady background presence of mud (e.g., Green et al., 2000; van de Kreeke & Hibma, 2005). Concentrations of both classes of sediment were kept within the linear range of response for each instrument (<5,000 mg/L of mud and <50,000 mg/L of sand for the OBS (J. Downing, 2006) and <5,000 mg/L for the ADV (Salehi & Strom, 2011) to avoid ambiguity in the readings. Precise details of the suspended sediment concentrations and sand fractions in each experiment are provided in Appendix A and experimental protocols are outlined in Supporting Information.

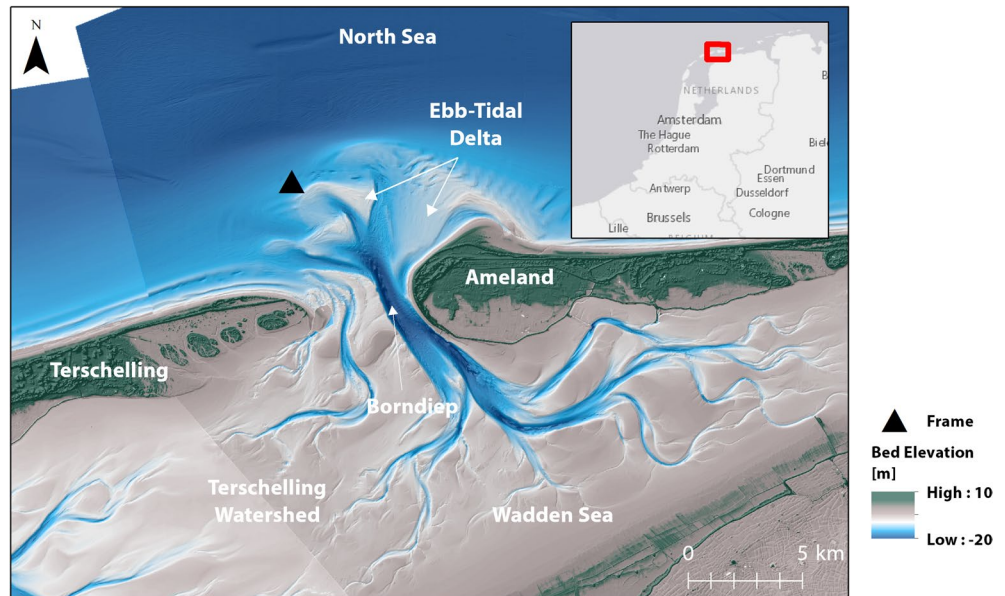


Figure 2. Overview of measurements during the September 2017 field measurement campaign at Ameland Inlet, including the frame (AZG-F4) bearing the instruments used in this study. Bathymetry source: Rijkswaterstaat Vaklodgingen. Elevation source: Actueel Hoogtebestand Nederland (AHN), Rijkswaterstaat. Basemap sources: Esri, HERE, Garmin, ©OpenStreetMap contributors, and the GIS user community.

Vertical concentration gradients were observed within the tank for 200 μm sand, but all instruments and samples measured within 10 cm of the same elevation, leading to comparable sample and sensor data. The propeller at the bottom of the tank was set to a speed of 175 rpm to provide high turbulent shear between $G = 30$ and 100 s^{-1} , maximizing resuspension and mixture homogeneity while minimizing the formation of bubbles.

In Experiments 1 and 2, acoustic backscatter was measured using a Nortek Vector ADV (Nortek AS, 2005), operating at a frequency of 6 MHz, and sampling at 32 Hz (8 Hz in Experiment 2), 20 cm beneath the water surface (25 cm in Experiment 2). *OBS* was measured in Experiment 1 using a Wetlabs combined FLuorometer and turbidity sensor (Nephelometric Turbidity Units) (FLNTU) WET Labs Inc (2019), sampling at 1 Hz, 20 cm beneath the water surface. In order to exclude data points below the sensor's detection limits for coarser particles, turbidity data below 0.9 NTU are discarded from the study. In Experiment 2, a Campbell OBS-3+ (Campbell Scientific Inc., 2014) was used instead, with similar properties to the Wetlabs FLNTU. To calibrate the optical and acoustic measurements, an external pump was connected to the tank 30 cm beneath the surface to extract suspended sediment samples. The instruments were arranged to avoid mutual interference but while sampling a similar elevation and hence similar sediment concentrations. All sensors were operated in continuous recording mode for the duration of each experiment, and statistics were computed over a 10–11-min period at each sediment concentration level. The median SNR of the three ADV beams and median *OBS* output were then used to calculate the relative optical-acoustic backscatter index SCI from Equation 9.

2.2. In Situ Measurements

Ameland Inlet is located in the Netherlands between the sandy barrier islands of Terschelling and Ameland, connecting the North Sea with the Dutch Wadden Sea (Figure 2). The inlet is characterized by a 30-m deep main channel (the “Borndiep”) on its eastern side and a shifting complex of shoals and channels on its west side. There is a large and highly dynamic ebb-tidal delta complex on the seaward side of the inlet and a shallow backbarrier basin environment of intertidal shoals and flats on the landward side (the Wadden Sea) (Elias et al., 2019; Lenstra et al., 2019). The seabed of the ebb-tidal delta of the inlet is mainly well-sorted sand (mean $d_{50} = 211 \mu\text{m}$, $n = 165$) with mud content generally $<1\%$, whereas the Wadden Sea has a mud

content up to 20% at its landward edge and on the intertidal flats separating Ameland Inlet from adjacent tidal basins (Pearson et al., 2019; Rijkswaterstaat, 1999). Samples with mud content of ~5% can also be found on the North Sea bed beyond the distal end of the ebb-tidal delta.

A field measurement campaign was carried out from August 29 to October 9, 2017, with the goal of characterizing hydrodynamic and sediment transport processes in the inlet and on its ebb-tidal delta (Brakenhoff et al., 2020; De Wit et al., 2019; Reniers et al., 2019; van der Werf et al., 2019; Van Prooijen et al., 2020). Measurements of flow, waves, SPM, bedform dynamics, and water quality were made at four locations across the site. Measurements considered in this study were obtained at frame AZG-F4 (Figure 2), at the distal end of the ebb-tidal delta, approximately 8 m deep.

As with the laboratory experiments in Section 2.1, acoustic backscatter was measured using three Nortek Vector ADVs (Nortek AS, 2005), operating at a frequency of 6 MHz, and sampling at 16 Hz, 20, 50, and 78 cm above the seabed. The median SNR of acoustic backscatter was taken over 30 min bursts for the deployment period as per Ha et al. (2009).

OBS was measured using four Campbell OBS-3+ (Campbell Scientific Inc., 2014), sampling at 16 Hz, 20, 30, 50, and 78 cm above the seabed. The *OBS* was initially calibrated using sandy sediment obtained from the seabed adjacent to the measurement frame, as is frequently done in practice (Fettweis et al., 2019; Paphitis & Collins, 2005). However, there is still concern that calibration using bed material can be inappropriate and error-prone if there are significant differences between the bed sediment and material in suspension (Bass et al., 2007; Beamsley et al., 2001; Kineke & Sternberg, 1992; Öztürk, 2017; Su et al., 2016), as expected at our field site. On this basis, the original calibration was discarded when it was recognized that the additional presence of suspended sediment significantly finer than the bed sediment made interpretation ambiguous. Thus, the uncalibrated *OBS* signal is presented here in volts. The median *OBS* signal over 30 min bursts was used.

Near-bed hydrodynamic conditions during the monitoring period were measured using a high-resolution downward-looking Nortek Aquadopp acoustic doppler current profiler (ADCP-HR) (Nortek AS, 2008). The ADCP sampled at a rate of 4 Hz in 30 min bursts. These measurements were averaged over the water column between the sensor and the bed (approximately 0.5 m, depending on field conditions) and then median velocities were calculated for each 30 min burst interval. Bed shear stresses due to the influence of waves and currents were calculated separately using the method of Soulsby (1997) (with default parameter settings) to give an indication of the potential for local bed material to be resuspended at the frame. For simplicity, we do not consider the effect of combined wave-current bed shear stresses here, which likely underestimates the frequency of sediment resuspension.

To assess the intratidal variation of the field measurements, we classified each 30 min burst into flood tide, high water slack (HWS), ebb tide, and low water slack (LWS) based on an analysis of tidal currents (Pearson et al., 2019). At the measurement site, the major axis of flow is almost exactly in an east-west direction. Thus, eastward (0° – 179°) currents exceeding 0.1 m/s were classified as flood, and westward (180° – 359°) currents exceeding that threshold as ebb. Velocities below that threshold with positive water surface elevations (with respect to mean water level) were classified as HWS, and with negative water surface elevations as LWS.

3. Results

3.1. Laboratory Experiments

3.1.1. Optical and Acoustic Backscatter

We consider the joint response of the optical and acoustic sensors to various sand/fine sediment mixtures: from purely mud suspensions to purely sand suspensions and with varying total concentrations (Figure 3). Optical turbidity values are recorded in NTU or volts (Experiments 1 and 2, respectively) depending on the instrument deployed. Readings in volts are first normalized in equivalent NTU using an offset value in log space (constant for all Experiment 2 *OBS* data), so that their values are aligned in Experiments 1 and 2 for purely mud suspension conditions.

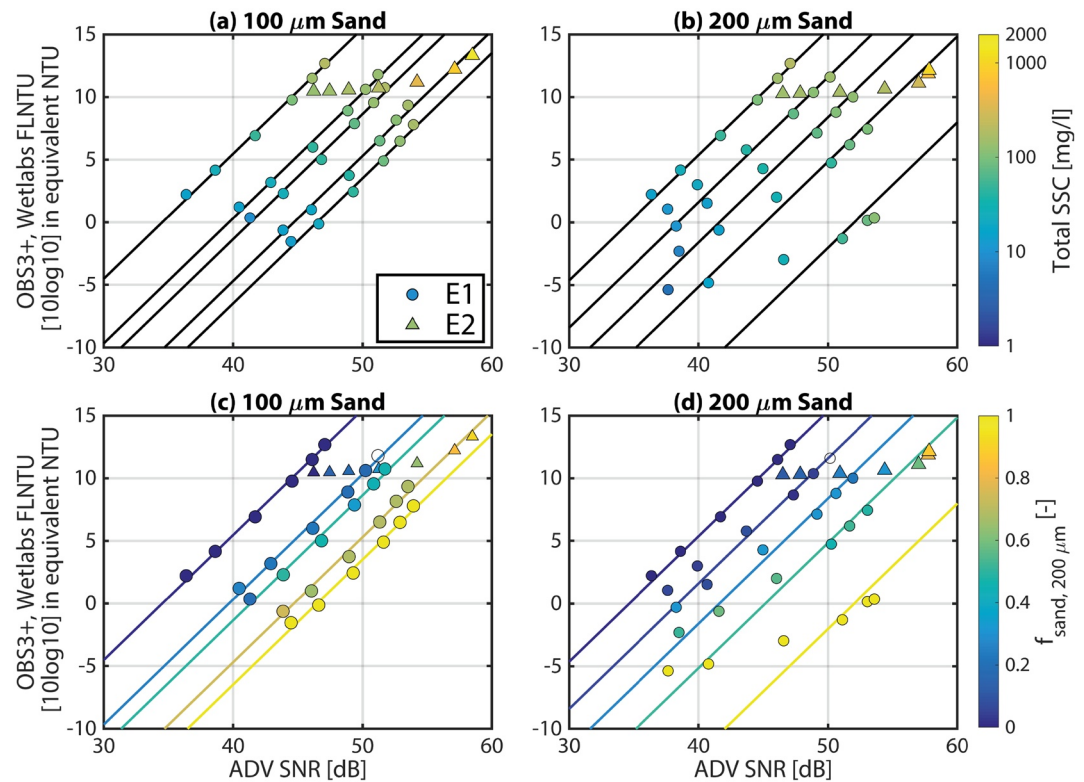


Figure 3. Median acoustic (ADV SNR) and optical backscatter (OBS) as a function of total suspended sediment concentration (a, b) and suspended sand fraction (f_{sand}) in the laboratory experiments (c, d). (a, c) Experiments with 100 μm sand. (b, d) Experiments with 200 μm sand. Data from Experiment 1 (E1) measured with a Wetlabs FLNTU are marked with circles ($n = 30$), while data from Experiment 2 (E2), measured with an OBS-3+, are marked with triangles ($n = 7$). Black and colored lines indicate constant f_{sand} contours. ADV, acoustic Doppler velocimeter; SNR, signal-to-noise ratio.

Results from Experiment 1 for 100 μm sand (Figures 3a and 3c) show that the sensors' response is linear in $\log_{10}(\text{OBS})/\text{ADV SNR}$ space. This is valid for a range of total sediment concentration (from 15 to 200 mg/L), such that $10 \log_{10}(\text{OBS}) = \text{SNR} + \text{SCI}$, confirming the theoretical relationship (Equation 9). Increasing the sand fraction (f_{sand}) leads to a shift in the data alignment for the different conditions, but lines are still parallel (Figure 3c). That is, for a given ADV SNR value, the optical turbidity value increases as SPM becomes finer. Conversely, for a given optical turbidity value, ADV SNR increases as SPM become sandier. Experiment 2 independently tested a larger total SSC gradient, increasing the sand content from 0% to 100% and total sediment concentration from 135 to 1603 mg/L, while progressively adding sand (Figures 3a and 3c). These results are in full agreement with Experiment 1, with their data points matching the corresponding sand/mud ratio contours as sand content increases.

Similar results are observed for 200 μm sands: $\log_{10}(\text{OBS})/\text{ADV}$ pairs are aligned for a given sand content, and these lines are organized parallel to each other (Figures 3b and 3d). For similar turbidity values, the SNR signal is stronger for 200 μm sand than for 100 μm sand (Figures 3a and 3b). However, deviations from alignment are observed when sand content dominates (i.e., $f_{sand} > 50\%$) and total concentration is low (i.e., $\text{SSC} \leq 50 \text{ mg/L}$) (Figures 3b and 3d). This bias corresponds to the poor sensitivity of the optical sensor to detect low 200 μm particle concentrations, when there are few scatterers in suspension. In such conditions, recorded NTU values range from 0.1 to 0.9 NTU, close to the sensor resolution and lower detection limit.

The measurements in Figure 3 are time-averaged values (see Supporting Information for full protocols), and we describe signal variability using the coefficient of variation ($CV = \sigma/\mu$). In Experiment 1, Wetlabs FLNTU signals are more variable when sand particles get coarser (from $CV = 2\%$ – 3% for pure mud to 3% – 16% for pure 100 μm sand and 5% – 22% for pure 200 μm sand) and 2% – 9% for sand–mud mixtures. ADV SNR

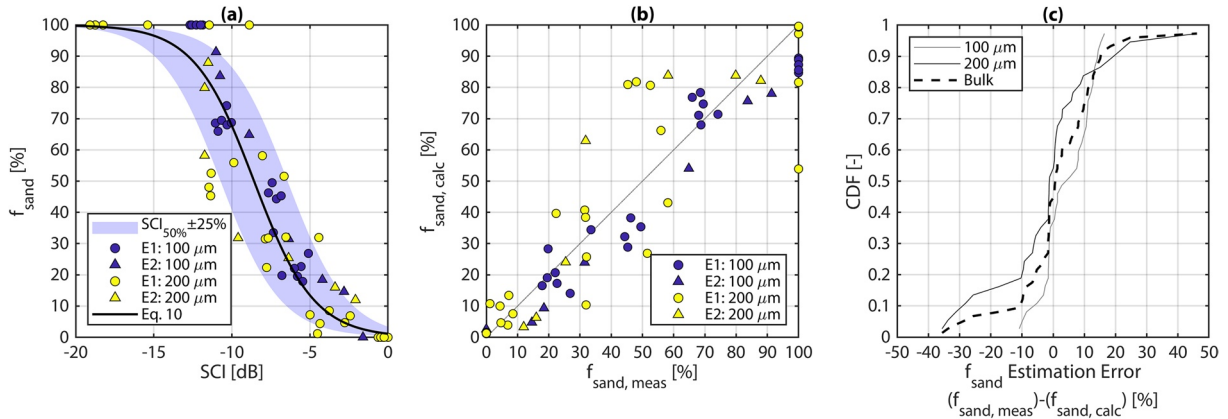


Figure 4. Fraction of sand in total suspended sediment (f_{sand}), calculated from the sediment composition index (SCI). (a) f_{sand} as a function of SCI, with Equation 10 fit to both grain sizes in bulk ($SCI_{50\%} = -8.58$). Blue bands indicate the envelope of uncertainty in f_{sand} , varying $SCI_{50\%}$ by $\pm 25\%$. Experiments 1 and 2 (E1 and E2, respectively) are indicated, along with the sand grain size used in each experiment ($R_{100}^2 = 0.957$, $R_{200}^2 = 0.806$, and $R_{bulk}^2 = 0.884$). (b) Comparison of experimentally measured $f_{sand, meas}$ with $f_{sand, calc}$ determined using Equation 10. (c) Cumulative distribution function (CDF) of sand fraction estimation error ($f_{sand, meas} - f_{sand, calc}$) for each sand grain size class and for all classes combined in bulk.

variability is less ($CV < 6\%$ for mud, 100 μm sand, and 100 μm sand–mud mixtures) and generally decreases with increasing concentration. The highest ADV SNR variability was seen for low concentrations of pure 200 μm sand (CV up to 20%). Sand–mud mixtures (200 μm) have CV ranging from 5% to 13% in Experiment 1. For sand–mud mixtures in Experiment 2, OBS signal variability is between 6% and 12% and ADV SNR variability is between 2% and 5%. As with Experiment 1, mixtures with 200 μm sand showed higher signal variability than mixtures with 100 μm sand in Experiment 2.

3.1.2. Sediment Composition Index

We derived the SCI for the laboratory measurements using Equation 9, and it is shown to be an appropriate proxy for evaluating the sand content (Figure 4a). As a first step toward a generic SCI, we propose to normalize SCI such that $SCI = 0$ in purely muddy conditions.

To understand the relationship between the derived SCI and the actual sediment composition, we compare f_{sand} with SCI from both experiments and grain size classes and find a negative correlation (Figure 4a). A hyperbolic tangent was fit to the data (Equation 10) because f_{sand} should asymptotically reach 0% for maximum SCI (minimum acoustic response, maximum optical response, no sand, only mud) and should tend asymptotically toward 100% for minimum SCI (maximum acoustic response, minimum optical response, only sand, no mud).

$$f_{sand} = \left(\frac{1}{2} + \frac{1}{2} \tanh \left[\frac{-(SCI - SCI_{50\%})}{\Delta SCI} \right] \right) \cdot 100\% \quad (10)$$

where $SCI_{50\%}$ is a constant corresponding to a mixture of 50% sand and 50% mud. It is equal to -8.03 when fitting only 100 μm sand ($R_{100\mu\text{m}}^2 = 0.954$), -9.63 for 200 μm sand ($R_{200\mu\text{m}}^2 = 0.848$), and -8.58 when both grain sizes are fit in bulk ($R_{bulk}^2 = 0.884$). For the analyses in the rest of this study, we consider $SCI_{50\%} = -8.58$, $\Delta SCI = 3.85$ and indicates the width in variation. Equation 10 allows us to deepen the interpretation of SCI by directly predicting f_{sand} (and by extension, $f_{mud} = 1 - f_{sand}$). It shows good predictive skill when compared with measured f_{sand} for both experiments and grain size classes ($R_{100}^2 = 0.957$, $R_{200}^2 = 0.806$, and $R_{bulk}^2 = 0.884$) (Figure 4b). The bulk prediction is accurate for 200 μm sands, as 70% of the calculated sand fractions are associated with an absolute error lower than $\pm 10\%$. Results are the best for 100 μm sand, with more than 85% of the samples estimated with an absolute error below $\pm 10\%$. In case the sand distribution is not known, we also investigated the SCI response to sand content when merging all experimental data

(Figure 4c). This bulk index still performs well, with 70% of the calculations with errors within $\pm 10\%$, although the error range is slightly larger, between -30% and $+20\%$.

3.2. In Situ Measurements

3.2.1. Hydrodynamic Conditions

The measurements from Ameland ebb-tidal delta span 40 days (August 29 to October 8, 2017) or approximately 2.5 spring–neap cycles (Figure 5a). There are two minor storms ($H_s \approx 1$ m) on August 30 and September 7 and two major storms ($H_s > 4$ m), *Sebastian* (September 14, during neap tide) and *Xavier* (October 6, during spring tide).

Spring tide occurs around September 10, 20, and October 7 (corresponding to the larger tidal range in Figure 5a). Under calmer conditions, bed shear stresses due to currents ($\tau_{b,c}$) exceed the critical threshold for local sand ($\tau_{cr,211 \mu m} = 0.18$ Pa, derived using Soulsby, 1997) only during spring flood tides (Figures 5c and 6f). These periods with currents strong enough to resuspend or advect sand correspond to flood and ebb stages of the tidal cycle (Figures 5a and 6b).

Wave-induced bed shear stress $\tau_{b,w}$ is greatest during the storms (Figures 5b and 6c), exceeding $\tau_{cr,211 \mu m}$. High bed shear stresses due to currents ($\tau_{b,c}$) are also observed during the two major storms, likely due to wind-induced storm surge and wave-driven currents (Figure 5b). During *Storm Sebastian* on September 14, eastward currents during the peak of the storm were so strong and persistent that the tide did not reverse (no ebb occurred for nearly 24 h). During storm periods, $\tau_{b,w}$ is greatest at low tide.

3.2.2. Optical and Acoustic Backscatter

Over the total deployment period, *OBS* measurements show strong tidal variation and a response to individual storm events (Figures 5d and 6h). The largest ADV readings occur during spring tide and the peaks of the two largest storms (Figures 5e, 6i, and 6j), while the lowest ADV SNR readings tend to correspond to calmer periods with low wave stress (Figures 5e and 6j).

During *Storm Sebastian* on September 12–16, both SNR and *OBS* signals strongly increase and tidal variation is weak for the next two tidal cycles (Figures 6g and 6i). Both signals remain relatively high but noisy, and higher background (minimum) readings persist for about a week after the storm.

During the calm spring tidal period from September 21 to 25, the influence of waves is minimal and the intratidal dynamics are clear (Figures 6h and 6j). The *OBS* signal shows strong M2 (semidiurnal) tidal oscillations peaking around LWS. Conversely, ADV SNR shows mixed M2 and M4 (quarter-diurnal) tidal variation, peaking at flood tide and to a lesser degree at ebb. ADV SNR is lowest at HWS. The calm period from September 28 to October 2 coincides with neap tide and exhibits similar dynamics to the prestorm period at the beginning of the monitoring period, albeit with lower background *OBS* and ADV SNR levels and reduced intratidal variability.

3.2.3. Sediment Composition Index and f_{sand}

Suspended sediment composition was estimated from the optical and acoustic backscatter readings. SCI was calculated with Equation 9, using the *OBS* and ADV SNR measurements 50 cm above the bed. SCI was offset to zero by subtracting its 99th percentile value. As in the laboratory experiments, this corresponds to a condition when sand is not likely present. This assumption is corroborated by the calm hydrodynamic conditions during moments of high SCI. We then applied Equation 10 with $SCI_{50\%} = -8.58$ (fit to both 100 and 200 μm sand) to the SCI time series including the confidence bands to approximate the fraction of sand in suspension (f_{sand}).

At subtidal time scales, SCI is lower during storms and spring tides (e.g., Figures 6k and 6l). SCI reaches its lowest observed values during spring tide, during both calm and stormy periods (Figure 5b). By contrast, it is highest during calm conditions and neap tide (e.g., Figure 5f from September 28 to October 2). SCI is much more dynamic at spring tide, its standard deviation nearly doubling when compared to neap tide.

Over the course of a tidal cycle, SCI typically followed a mixed M2 and M4 pattern. The M4 signal has minima at flood and ebb tide and is especially pronounced during spring tidal conditions. Superimposed on this

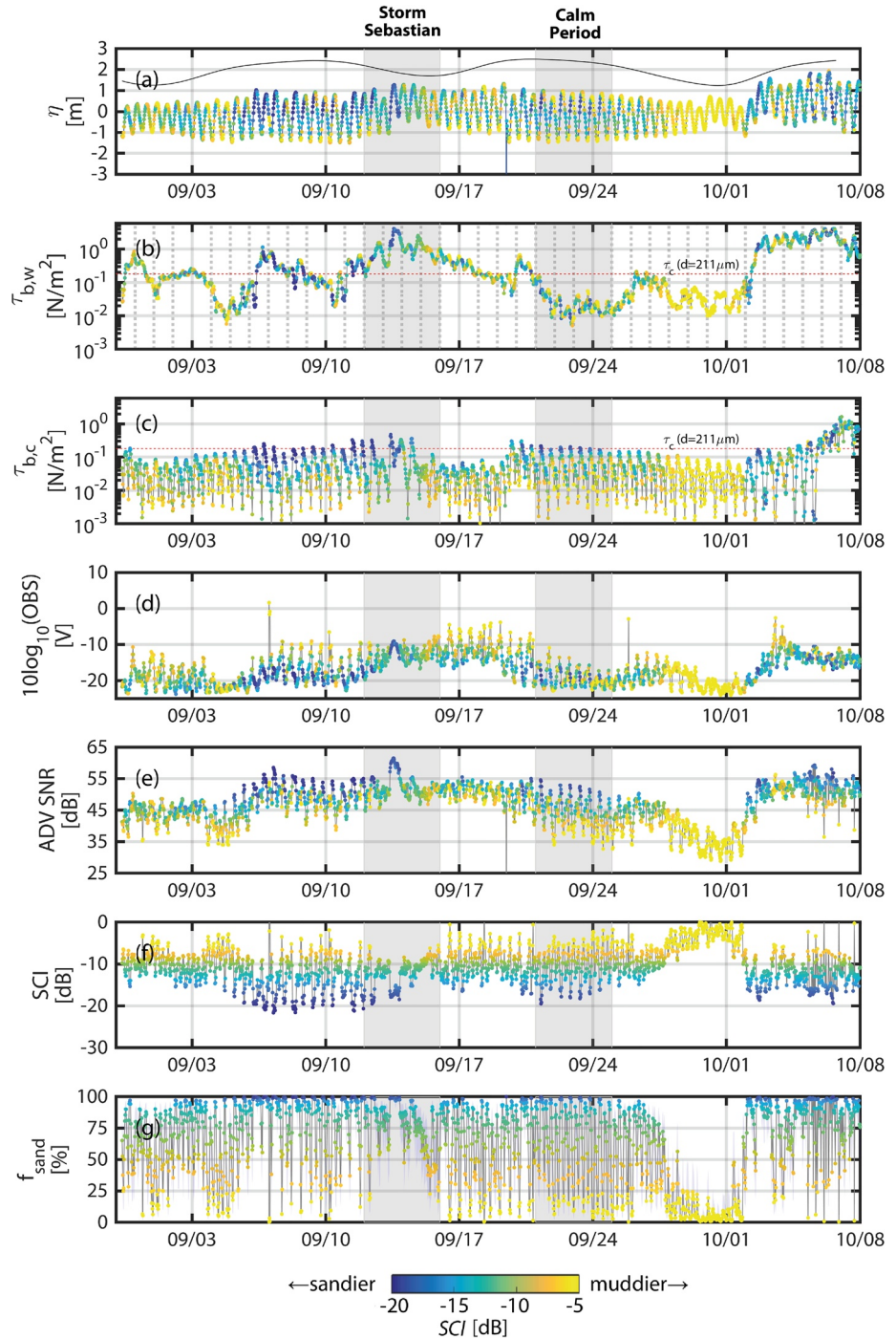


Figure 5. Time series of hydrodynamic conditions and backscatter at Ameland ebb-tidal delta Frame 4, with dot color indicating relative optical-acoustic backscatter index SCI. Higher SCI (lighter yellow colors) suggest relatively higher mud content, and lower SCI (darker blue colors) suggest relatively higher sand content. (a) Water level relative to the mean depth during the deployment period (8.3 m). The tidal range (indicated with a solid black line) shows spring tide (high values) and neap tide (low values). (b) Bed shear stress due to waves ($\tau_{b,w}$). The critical shear stress for local sand ($\tau_{cr,211\ \mu m} = 0.18\ \text{Pa}$) is indicated with a dashed line. (c) Bed shear stress due to currents ($\tau_{b,c}$). (d) Log of optical backscatter measured 50 cm above the bed. (e) Acoustic backscatter (signal-to-noise ratio, SNR) measured 50 cm above the bed. (f) Relative optical-acoustic backscatter index SCI. (g) Fraction of sand in total suspended sediment (f_{sand}) calculated from SCI using Equation 10. SCI, sediment composition index.

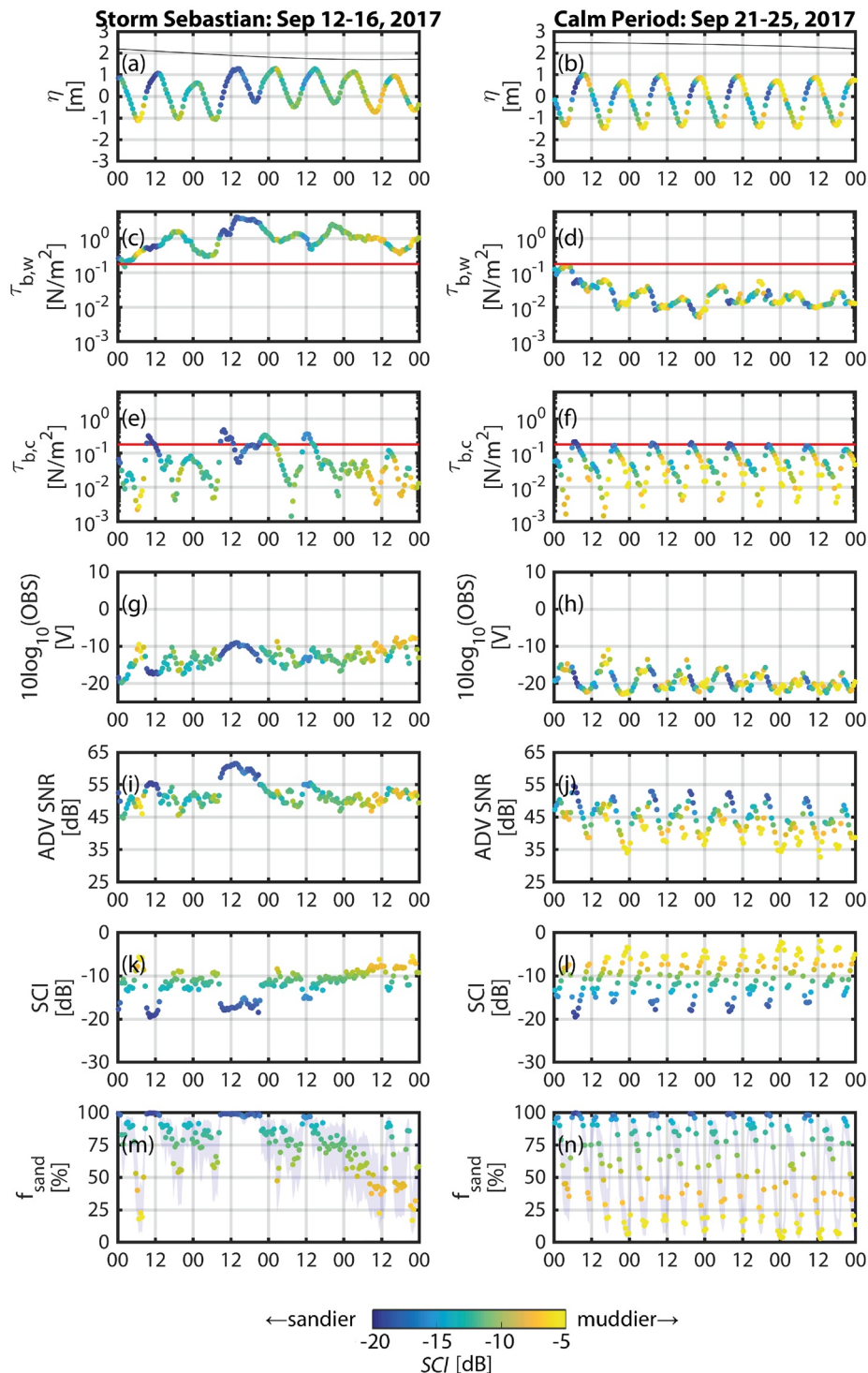


Figure 6. Time series of hydrodynamic conditions and backscatter at Ameland ebb-tidal delta Frame 4, focusing on Storm Sebastian (September 12–16) and a calmer period during spring tide (September 21–25). Dot color indicates relative optical-acoustic backscatter index SCI. Higher SCI (lighter yellow colors) suggest relatively higher mud content, and lower SCI (darker blue colors) suggest relatively higher sand content. (a, b) Water level (η) relative to the mean depth during the deployment period (8.3 m). The tidal range (indicated with a solid black line) shows spring tide (high values) and neap tide (low values). (c, d) Bed shear stress due to waves ($\tau_{b,w}$). The critical shear stress for local sand ($\tau_{cr,211\ \mu\text{m}} = 0.18\ \text{Pa}$) is indicated with a dashed line. (e, f) Bed shear stress due to currents ($\tau_{b,c}$). (g, h) Log of optical backscatter. (i, j) Acoustic backscatter (signal-to-noise ratio, SNR). (k, l) Relative optical-acoustic backscatter index SCI. (m, n) Fraction of sand in total suspended sediment (f_{sand}) calculated from SCI using Equation 10. SCI, sediment composition index.

is an M2 variation with its peak centered at ebb tide. The combination of these two signals results in minimal SCI at flood tide when $\tau_{b,c}$ is high, then a peak at HWS when $\tau_{b,c}$ is low (Figure 6l). This is followed by a sharp drop to a secondary minimum at ebb tide (when $\tau_{b,c}$ increases again), and then a gradual rise to another peak at LWS. The cycle completes with another rapid decline in SCI at flood tide as currents strengthen. Although SCI nearly always peaks at slack water, the maximum varies between LWS (e.g., September 8–10) and HWS (e.g., September 21–25).

SPM composition varied throughout the tidal cycle, with distinct differences observed between periods of higher flow (i.e., ebb and flood) and periods of lower flow (i.e., slack water). SPM is dominated by sand at ebb and flood tide, when $f_{sand} > 75\%$ (Figure 6n). Conversely, the suspension consists primarily of mud at high and LWS ($f_{sand} < 25\%$). f_{sand} follows an M4 signal, with only weak M2 variations compared to SCI.

The presence of waves (indicated by higher wave-induced bed shear stress $\tau_{b,w}$) was often associated with lower SCI (Figure 5b). During Storm Sebastian on September 13, SCI drops during the peak in the storm and loses its characteristic M2–M4 tidal variation for several days (Figure 6k). This corresponds to a period of mainly sand in suspension ($f_{sand} > 75\%$), with f_{sand} approaching 100% at the peak of the storm (Figure 6m). The proportion of mud in suspension increases toward the end of the storm, and tidal variations in f_{sand} begin to return.

To further explore the influence of waves on tidal variations in relative optical-acoustic response, SCI is plotted as a function of wave ($\tau_{b,w}$) and current-related bed shear stresses ($\tau_{b,c}$) at each stage of the tidal cycle (Figure 7). We summarize the variability of SCI relative to wave and current forcings (shear stresses), separating results into flood and ebb-tidal phases. In this shear stress space, the dynamics of SCI are clearly structured. During calm flood tides ($\tau_{b,w} < \tau_{cr,211 \mu m}$), SCI ranges from 0 dB during weak currents to -22 dB during stronger currents. A similar pattern is observed during ebb, although generally $SCI > -15$ dB. This can be explained by the weaker $\tau_{b,c}$ during maximum ebb compared with during maximum flood. Both high and LWS are characterized by relatively high SCI (> -10 dB). SCI reaches < -12 dB during slack periods during wavy conditions. Larger wave-induced stresses are generally associated with $SCI < -5$ dB, although brief peaks in SCI can sometimes be observed during storms (Figure 5).

4. Discussion

4.1. Interpreting the Dynamics of the SCI

The SCI is a useful indicator of the relative fractions of sand and mud in suspension, as validated in laboratory experiments. Application of this index was demonstrated by interpreting the sediment dynamics on Ameland ebb-tidal delta in light of two main processes: resuspension of local sandy bed material by waves and strong tides and tidal advection of mud from locations outside the ebb-tidal delta. These processes explain the response of optical and acoustic backscatter measurements, and hence the corresponding dynamics of SCI.

At subtidal time scales (> 24 h), the dynamics of SCI can be explained in part by a fortnightly spring–neap cycle. The larger intratidal variation of SCI at spring tide is likely due to the increased resuspension of sand by stronger currents (Figure 5c) and to the greater advection of mud from nearby intertidal flats at late ebb and LWS, similarly to the observations of Weeks et al. (1993) and Fettweis et al. (1998) at other sites. Conversely, high SCI (and thus higher relative proportions of mud in suspension) coincides with the neap tide (e.g., September 28 to October 1) and with lower values of $\tau_{b,w}$ and $\tau_{b,c}$. Without sufficiently strong forcing to resuspend local sand ($\tau_b < \tau_{cr,211 \mu m} = 0.18$ Pa, derived using Soulsby, 1997), only mud can remain in suspension (Figure 5c).

The observed intratidal variation in SCI (Figure 6l) can be explained by the local hydrodynamics and sedimentary environment and is summarized conceptually for a generic sandy tidal inlet or ebb-tidal delta with a muddy inner basin in Figure 8. At flood and ebb tide, strong currents are capable of resuspending sand from the local seabed or advecting it from elsewhere nearby, so the corresponding SCI values decrease. Conversely, when sand settles out at slack water, only the suspended mud remains in the water column, explaining the increase in SCI value at that time. The result is an M4 signal with minima at flood and ebb

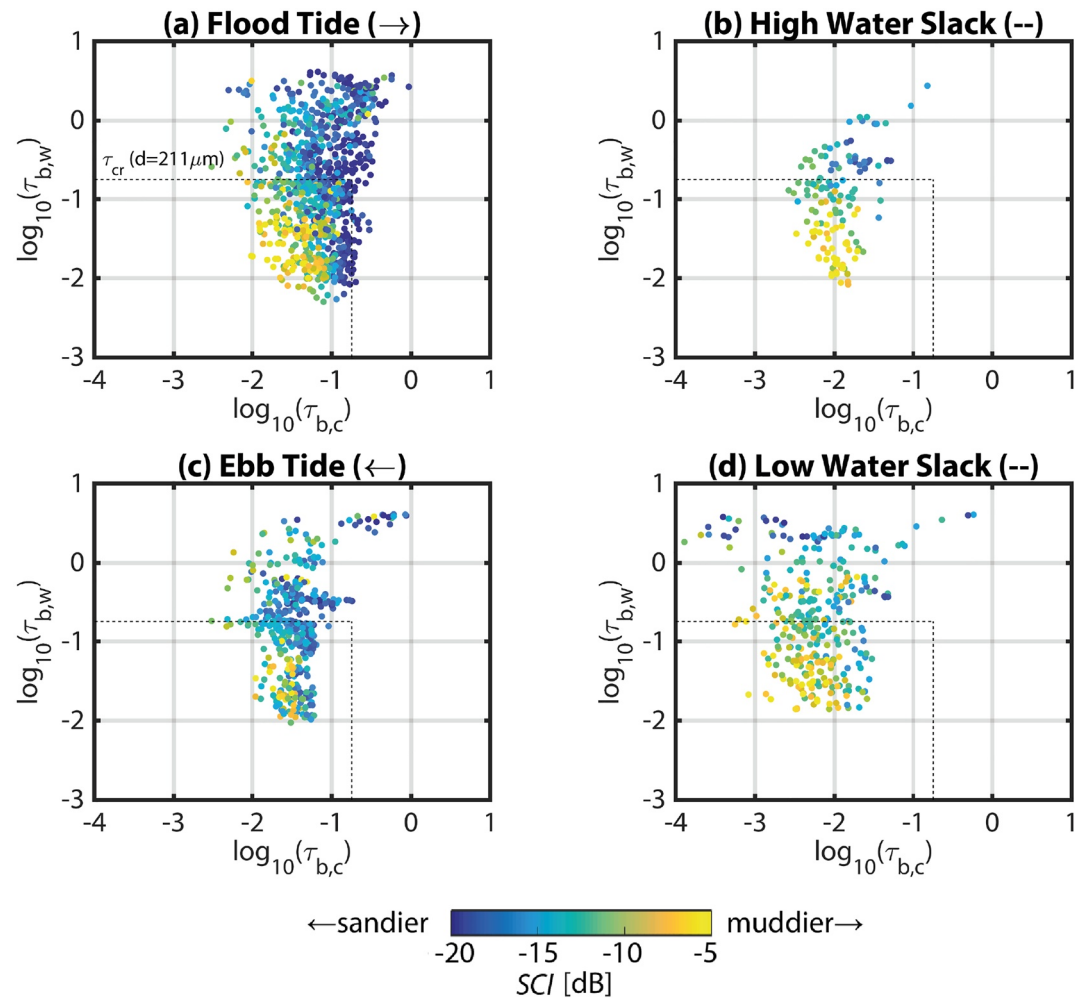


Figure 7. Sediment composition index SCI (in color) as a function of wave shear stress (vertical axes) and current shear stress (horizontal axes), at four different stages of the tidal cycle. (a) Flood tide ($u > 0.1$ m/s and to the east), (b) high water slack ($u < 0.1$ m/s and at high water), (c) ebb tide ($u > 0.1$ m/s and to the west), and (d) low water slack ($u < 0.1$ m/s and at low water). The critical shear stress for local $211 \mu\text{m}$ sand (0.18 Pa) is plotted for reference as a dotted line. Bed shear stresses were computed using Soulsby (1997).

tide. This relationship between local resuspension and local current velocities is also observed by Lavelle et al. (1984), Weeks et al. (1993), Bass et al. (2002), and van de Kreeke & Hibma (2005).

Modulating the M4 SCI signal is an M2 signal with its maximum centered at ebb tide. This M2 signal can be explained by the semidiurnal migration of a strong landward mud concentration gradient in the channels of Ameland basin (Postma, 1961). Remote sensing indicates that this turbid water mass can be ejected several kilometers seaward of the inlet and across the ebb-tidal delta at ebb (Pearson et al., 2019), which causes the corresponding SCI to increase. This muddy water mass is then displaced by less turbid oceanic water on the flood tide, so SCI decreases again. This semidiurnal transport pattern is widely observed at other sites where there is a persistent gradient in suspended mud concentration (Bass et al., 2002; Green et al., 2000; van de Kreeke & Hibma, 2005; Weeks et al., 1993).

To fully explain the SCI dynamics at Ameland, the episodic influence of storms must also be accounted for. If waves are sufficiently large ($\tau_{b,w} > \tau_{cr,211\mu\text{m}}$), then the majority of local sand can be mobilized, which can result in low values of SCI regardless of the tidal stage. Conversely, the periods with the lowest SCI (suggesting lower proportions of sand in suspension and relatively more mud) coincide mainly with periods of low wave action (e.g., September 28 to October 1).

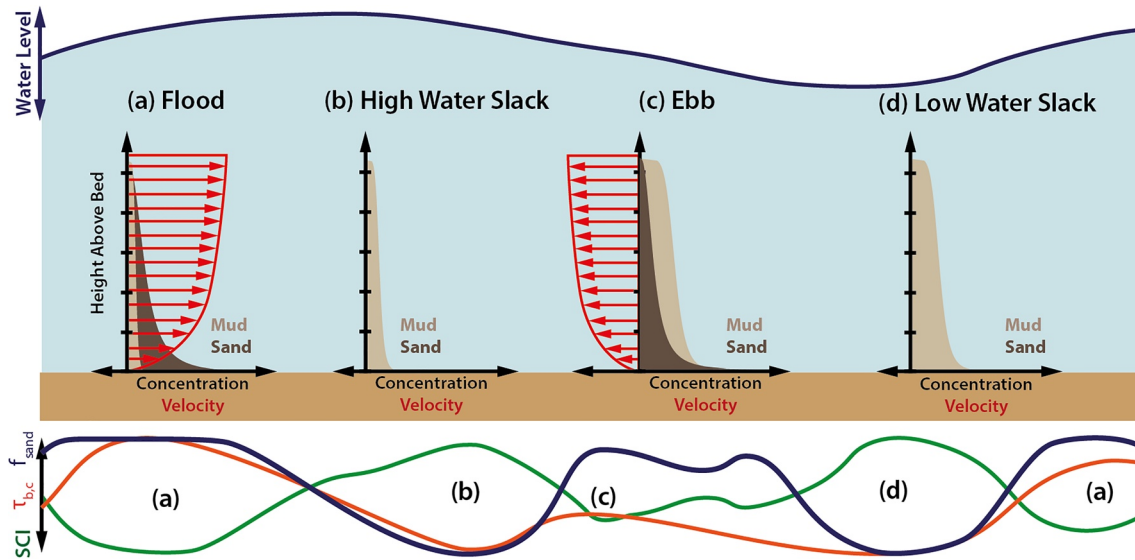


Figure 8. Conceptual model of tidally driven mixed sand–mud sediment transport at a sandy tidal inlet or ebb-tidal delta with a muddy inner basin. A normalized example time series of sediment composition index (SCI), bed shear stress due to currents ($\tau_{b,c}$), and fraction of sand in suspension (f_{sand}) over a tidal cycle are indicated below. (a) At flood tide, strong currents locally resuspend sand but carry few mud particles from the sea, so SCI is low. (b) At HWS, currents are too weak to mobilize sand, so total concentrations are relatively low and consist only of mud, so SCI is higher. (c) At ebb tide, strong currents locally resuspend sand, though less than at flood tide, so SCI decreases again. These ebb currents also carry with them mud particles from the muddy and biologically productive inner basin. (d) At low water slack, currents are too weak to mobilize sand, leaving only the mud advected from the inner basin at ebb, which begins to settle, resulting in higher SCI.

During periods with large waves, SCI may be influenced not just by an increased capacity for local resuspension of sand but also by wind and wave-induced mud resuspension. This is reflected in the SCI signal during Storm Sebastian (Figure 6). Even when bed shear stresses due to waves and currents greatly exceed $\tau_{cr,211 \mu m}$, SCI seldom drops below -15 dB and f_{sand} remains between 50% and 90% for most of the storm. In the latter half of the storm, f_{sand} decreases as sand settles out, while mud remains in suspension. This mud can originate from two locations: the Wadden Sea tidal basin and the bed of the North Sea. During storms, tidal flats in Ameland basin may easily lose the surface layers of sediment deposited in calm periods (Postma, 1961). In a similar case study, Green et al. (2000) found that wave activity on nearby intertidal flats was the principal determinant of suspended mud load advected through a tidal channel. However, storms may also remobilize mud which accumulates in the bed of the North Sea (Flores et al., 2017; Hendriks et al., 2020; Van Der Hout et al., 2017). Instantaneous bed shear stress does not tell the whole story of suspended sediment composition: it is also necessary to account for spatial and temporal variations in the supply of mud.

Our interpretation of SCI based on theoretical considerations and the laboratory results are fully supported by the local hydrodynamics and sedimentological context. SCI thus provides a novel and valuable characterization of the suspended sediment dynamics on Ameland ebb-tidal delta. This metric is especially useful for mixed sediment environments like Ameland where optical and acoustic measurements are otherwise ambiguous when viewed in isolation.

4.2. Limitations and Outlook

Having been conceptually validated by laboratory and field measurements, there are many opportunities for further developing the SCI and improving its applicability. The next steps toward a more quantitative evaluation of sediment composition lie in the accumulation of larger data sets and in quantifying the component of SCI specific to the instruments being used (the c_{instr} term of Equation 8, which is invariant with SPM).

For a more generic SCI, we propose a reference calibration of optical and acoustic sensors to evaluate the instrument constant c_{instr} (Equation 8), using NTU/BTU (formazin calibration) for optical systems, and monodispersed glass beads for acoustic particles, similarly to the calibration procedure for an acoustic backscatter system (e.g., Thorne & Meral, 2008). With calibrated scatterers, the sonar equation (Equation 4) can be fully

evaluated, the instrument constant c_{instr} is the only unknown. Acoustic backscatter is sensitive to the acoustic frequency of the transducers: the SCI dynamics will be different from 1 to 6 MHz sensors, because each sensor will respond differently to sediment of a given grain size and concentration. Similarly, optical sensors will provide different NTU values depending on whether the optical sensor is based on backscatter (e.g., OBS-3+ [Campbell Scientific Inc., 2014], Seapoint [Seapoint Sensors Incorporated, 2013], or Wetlabs [WETLabs, 2010]) or side scattering (e.g., YSI 6600 [YSI Incorporated, 2012]). Many additional laboratory experiments would be required in order to determine c_{instr} and make a full set of conversion factors for each type of instrument. By applying these calibrations, SCI could become generic, at least for similar instruments. However, even without quantifying c_{instr} directly, SCI provides useful information on suspended sediment composition when its dynamics are considered in the context of local hydrodynamic and sedimentological conditions.

Additional laboratory experiments must be carried out with a wider variety of sediment mixtures and concentrations. We expect that most of the variability of SCI is caused to first order by the presence of sand in suspension, because sand has a relatively stronger influence on acoustic backscatter than flocs of comparable size (Thorne & Hurther, 2014). However, the influence of flocculation on the variability of SCI requires further investigation. Estimating how SCI would change in response to organic matter also remains an open question. Organic matter has different optical and acoustic backscatter characteristics from inorganic sediment (Boss et al., 2018; Hoitink & Hoekstra, 2005), so its presence will potentially affect SCI.

Field measurements should also be collected from sites with different sedimentary characteristics under a range of hydrodynamic conditions in order to generalize the conclusions of the present study and SCI – f_{sand} relationships like Equation 10. Samples pumped at regular intervals (e.g., Beamsley et al., 2001) or better yet, at moments triggered by specific turbidity levels, would provide a more representative basis for calibrating optical and acoustic measurements. Fortunately, analyzing SCI dynamics of additional field sites is already possible, since optical and acoustic instruments are frequently paired together in the field (e.g., Colosimo et al., 2020; de Vet et al., 2020; Flores et al., 2018; Fugate & Friedrichs, 2002; Lin et al., 2020; Moura et al., 2011; Pomeroy et al., 2021; Voulgaris & Meyers, 2004; Zhu et al., 2019). Our approach thus gives added value to existing data sets by providing an additional, simple-to-calculate metric for interpreting sediment dynamics.

These additional efforts to make SCI more general and to better understand the underlying physics will strengthen the usefulness and applicability of the metric. This will lead to new insights into the dynamics of mixed sediment environments where ambiguity due to suspended sediment composition previously limited the information that could be obtained from optical and acoustic measurements.

This approach is most valuable in settings where it cannot be assumed that suspended sediment always has the same properties as the seabed. The majority of the world's coasts are heterogeneous sedimentary environments where these conditions may be found (Holland & Elmore, 2008). Even if ADV and OBS measurements are not available, the general principle of using differential optical and acoustic backscatter to disambiguate mixed sediment suspensions should still apply to pairs of other similar instruments. This would however require SCI-specific calibration experiments with the dedicated pair, similar to those performed in the present study. If applied in conjunction with instruments using different measurement principles (e.g., Laser In-Situ Scattering and Transmissometry [Agrawal & Pottsmith, 2000; Chapalain et al., 2019; P. S. Hill et al., 2011; Mikkelsen & Pejrup, 2001] or multifrequency acoustic backscatter sensors [J. R. Gray & Gartner, 2009; Moate & Thorne, 2009, 2012; Wilson & Hay, 2015]), SCI could yield even more insight into suspended sediment composition.

5. Conclusions

The SCI derived in this study quantifies the suspended sediment composition in mixed sediment environments. It does so using the relative intensity of optical and acoustic backscatter signals, as these two measurement techniques have different sensitivities to sand and mud (Equation 9). SCI can be used to estimate the fraction of sand and mud in suspension (f_{sand} and f_{mud}) in marine environments. Here, we verify the theoretical response of these optical and acoustic instruments in laboratory experiments. SCI is negatively correlated with the fraction of sand in suspension (Equation 10).

The SCI approach was successfully applied to in situ measurements on the ebb-tidal delta of Ameland Inlet in the Netherlands. SCI shows a clear M4 variation associated with suspension of local sand, modulated by

an M2 variation associated with suspended mud advected from the nearby Wadden Sea. Lower values of SCI (indicating a stronger acoustic response) and higher f_{sand} are observed under more energetic conditions when sand is expected to dominate the suspension (e.g., spring flood tide or strong wave conditions). Conversely, SCI increases (indicating a stronger optical response) and f_{sand} reduces in calmer conditions and at slack water, when the suspended sediment consists mainly of mud.

This approach reduces the ambiguity of suspended sediment composition in mixed sediment environments. Furthermore, it adds value to existing sets of measurements since simultaneous optical/acoustic measurements have frequently been carried out together in sediment transport studies. Being able to discern between different types of sediment in suspension will increase confidence in the interpretation of suspended sediment concentration measurements. This can ultimately improve estimates of sediment fluxes, leading to deeper understanding of coastal systems and enable better informed coastal management decision making.

Appendix A: Experimental Concentrations and Sand Fractions

A complete record of the sediment concentrations and sand fractions measured in Experiment 1 is provided in Table A1.

A complete record of the sediment concentrations and sand fractions measured in Experiment 2 is provided in Table A2.

Table A1
Summary of Sediment Concentrations in Experiment 1 (Bentonite With 100 and 200 μm Sand)

SSC_{target}	SSC_{actual}		f_{sand}	
	100 μm	200 μm	100 μm	200 μm
15	15.0	15.0	0.0	0.0
25	25.0	25.0	0.0	0.0
50	50.0	50.0	0.0	0.0
100	100.0	100.0	0.0	0.0
150	150.0	150.0	0.0	0.0
200	200.0	200.0	0.0	0.0
15	15.4	12.1	26.9	6.9
25	24.2	19.7	22.6	4.7
50	48.1	41.0	22.1	8.5
100	93.2	75.9	19.5	1.2
150	137.0	117.7	17.9	4.4
200	NaN	149.6	NaN	NaN
15	9.4	11.0	19.8	31.9
25	24.8	13.5	49.5	7.2
50	46.5	36.8	46.2	32.1
100	75.2	73.0	33.5	31.5
150	134.7	109.9	44.3	31.8
200	182.8	128.8	45.3	22.3
15	14.5	7.7	74.2	51.6
25	18.4	14.9	66.0	58.1
50	39.8	28.4	68.6	55.9
100	81.9	45.7	69.5	45.3
150	117.2	79.0	68.0	52.5
200	160.0	96.2	68.7	48.0

Table A1
Continued

SSC_{target}	SSC_{actual}		f_{sand}	
	100 μm	200 μm	100 μm	200 μm
15	14.0	4.8	100.0	100.0
25	20.5	15.6	100.0	100.0
50	45.5	27.8	100.0	100.0
100	85.7	52.8	100.0	100.0
150	126.2	76.9	100.0	100.0
200	175.6	115.1	100.0	100.0

Note. The left column indicates the target for each test, and the center column the actual SSC measured from pumped samples. The right columns indicate the sand content (f_{sand}) measured from pumped water samples.

Table A2

Summary of Sediment Concentrations in Experiment 2 (Estuarine Mud With 100 and 200 μm Sand)

Target	f_{sand} (%)		SSC_{fine}		SSC_{sand}		SSC_{total}	
	Measured		100 μm	200 μm	100 μm	200 μm	100 μm	
	100 μm	200 μm	100 μm	200 μm	100 μm	200 μm	100 μm	100 μm
0.0	0.0	12.0	134.9	127.9	0.0	17.4	134.9	145.3
10.0	14.6	16.0	128.1	127.1	21.9	24.2	150.0	151.3
25.0	18.5	25.4	133.0	123.9	30.1	42.2	163.1	166.1
50.0	31.5	31.8	134.0	125.8	61.6	58.7	195.6	184.5
75.0	64.9	58.2	132.4	123.6	244.3	172.2	376.7	295.8
90.0	83.7	79.9	131.4	124.6	674.2	494.5	805.6	619.1
95.0	91.4	87.9	138.6	128.6	1,464.4	936.0	1,603.0	1,064.6

Note. The left columns indicate the target and measured sand content (f_{sand}) for each test. The right columns indicate the fine sediment ($\leq 63 \mu\text{m}$), sand ($\geq 63 \mu\text{m}$), and total concentration in mg/L measured from pumped water samples.

Notation

b'	suspended particle property variable, dB
$b_{particle}$	variable function of SPM characteristics, dB
BI	volume backscatter strength, dB
c'	instrument characteristic constant, dB
c_{instr}	global (optical/acoustic) instrument-related constant, dB
C	constant including acoustic instrument-related and geometrical terms dB
C'	global acoustic constant, dB
CV	coefficient of variation
d	particle diameter, μm
d_{25}	particle diameter at 25th percentile, μm
d_{50}	median particle size, μm
d_{75}	particle diameter at 75th percentile, μm
E	emitted irradiance, W/cm^2
f_{mud}	fraction of mud in suspension ($100\% - f_{sand}$)
f_{sand}	fraction of sand in suspension ($100\% - f_{mud}$)
$f_{sand, calc}$	fraction of sand in suspension calculated using Equation 10
$f_{sand, meas}$	fraction of sand in suspension measured via water sample analysis
F	photon flux, W

G	turbulent shear, s^{-1}
H_s	significant wave height, m
k	wave number, m^{-1}
n	number of samples
N	number concentration of scatters, cm^{-3}
OBS	optical backscatter, V
Q_s	(back)scattering efficiency of the particles
r	one-way distance along path of acoustic pulse, m
R	one-way distance from acoustic transmitter to measurement volume, m
$R_{100\mu m}^2$	coefficient of determination for 100 μm sand
$R_{200\mu m}^2$	coefficient of determination for 200 μm sand
R_{bulk}^2	coefficient of determination for bulk sample of 100 and 200 μm sand
SCI	sediment composition index, dB
$SCI_{50\%}$	constant corresponding to a mixture of 50% sand and 50% mud, dB
SNR	signal-to-noise ratio (indicator of acoustic backscatter intensity), dB
SSC	suspended sediment mass concentration, kg/m^3
V	scattering volume, cm^3
\bar{V}_s	mean scattering volume, m^3
α_s	attenuation by suspended sediment, dB/m
α_w	absorption by water, dB/m
α_{OBS}	optical backscatter constant, $V \cdot m$
Δ_{SCI}	the width in variation of SCI, dB
η	water level relative to mean depth during measurement period, m
λ	light wavelength, μm
μ	mean
ρ_{floc}	floc density, kg/m^3
ρ_s	solid particle (dry) density, kg/m^3
σ	standard deviation
$\bar{\sigma}$	mean backscattering cross section, m^2
τ_b	bed shear stress, Pa
$\tau_{b,c}$	bed shear stress due to currents, Pa
$\tau_{b,w}$	bed shear stress due to waves, Pa
$\tau_{cr,211 \mu m}$	critical bed shear stress for 211 μm sand, Pa
ψ	spherical spreading constant

Acknowledgments

This work is part of the research program "Collaboration Program Water" with project number 14489 (SEAWAD), which is (partly) financed by NWO Domain Applied and Engineering Sciences. Special thanks to the Dutch Ministry of Infrastructure and Water Management (Rijkswaterstaat and Rijksrederij) for their ongoing support as part of the Kustgenese2.0 project. This work was also supported by ISblue project, Interdisciplinary graduate school for the blue planet (ANR-17-EURE-0015) and cofunded by a grant from the French government under the program "Investissements d'Avenir." DT was partly funded by the research project PHRESQUES 2, coordinated by the GIP Seine Aval and financed by the CPIER Vallée de Seine program. We are grateful to the two anonymous reviewers for their positive and constructive feedback, which has improved the quality of the manuscript.

Data Availability Statement

Data archiving for this study are currently underway, with some data already publicly available at 4TU. Centre for Research Data at <https://doi.org/10.4121/collection:seawad> Delft University of Technology et al. (2019). Details of this data set can be found in Van Prooijen et al. (2020) and van der Werf et al. (2019). Additional files from this study including laboratory experimental data are publicly available at: <https://doi.org/10.4121/14815893.v1>.

References

- Aagaard, T., Black, K. P., & Greenwood, B. (2002). Cross-shore suspended sediment transport in the surf zone: A field-based parameterization. *Marine Geology*, 185(3–4), 283–302. [https://doi.org/10.1016/S0025-3227\(02\)00193-7](https://doi.org/10.1016/S0025-3227(02)00193-7)
- Agrawal, Y. C., & Pottsmith, H. C. (2000). Instruments for particle size and settling velocity observations in sediment transport. *Marine Geology*, 168(1–4), 89–114. [https://doi.org/10.1016/S0025-3227\(00\)00044-X](https://doi.org/10.1016/S0025-3227(00)00044-X)
- Amoudry, L. O., & Souza, A. J. (2011). Deterministic coastal morphological and sediment transport modeling: A review and discussion. *Reviews of Geophysics*, 49, RG2002. <https://doi.org/10.1029/2010RG000341>
- Bass, S. J., Aldridge, J. N., McCave, I. N., & Vincent, C. E. (2002). Phase relationships between fine sediment suspensions and tidal currents in coastal seas. *Journal of Geophysical Research*, 107(10), 3146. <https://doi.org/10.1029/2001JC001269>
- Bass, S. J., McCave, I. N., Rees, J. M., & Vincent, C. E. (2007). Sand and mud flux estimates using acoustic and optical backscatter sensors: Measurements seaward of the Wash, southern North Sea. *Geological Society, London, Special Publications*, 274, 25–35. <https://doi.org/10.1144/GSL.SP.2007.274.01.04>

- Beamsley, B. J., Black, K. P., & Healy, T. (2001). Micro-scale pumped measurements of suspended sediment over a mixed sand/mud bed: Profiles, grain sizes and sediment diffusivity. *Journal of Coastal Research*, 34, 342–356.
- Boss, E., Sherwood, C. R., Hill, P., & Milligan, T. (2018). Advantages and limitations to the use of optical measurements to study sediment properties. *Applied Sciences*, 8(12), 2692. <https://doi.org/10.3390/app8122692>
- Boss, E., Slade, W., & Hill, P. (2009). Effect of particulate aggregation in aquatic environments on the beam attenuation and its utility as a proxy for particulate mass. *Optics Express*, 17(11), 9408. <https://doi.org/10.1364/oe.17.009408>
- Boss, E., Slade, W. H., Behrenfeld, M., & Dall'Olmo, G. (2009). Acceptance angle effects on the beam attenuation in the ocean. *Optics Express*, 17(3), 1535. <https://doi.org/10.1364/oe.17.001535>
- Brakenhoff, L., Kleinhans, M., Ruessink, G., & Vegt, M. (2020). Spatio-temporal characteristics of small-scale wave–current ripples on the Ameland ebb-tidal delta. *Earth Surface Processes and Landforms*, 45, 1248–1261. <https://doi.org/10.1002/esp.4802>
- Campbell Scientific Inc. (2014). *OBS-3+ and OBS300 suspended solids and turbidity monitors* (Tech. Rep.). Logan, UT: Campbell Scientific Inc.
- Chanson, H., Trevethan, M., & Aoki, S.-i. (2008). Acoustic Doppler velocimetry (ADV) in small estuary: Field experience and signal post-processing. *Flow Measurement and Instrumentation*, 19, 307–313. <https://doi.org/10.1016/j.flowmeasinst.2008.03.003>
- Chapalain, M., Verney, R., Fettweis, M., Jacquet, M., Le Berre, D., & Le Hir, P. (2019). Investigating suspended particulate matter in coastal waters using the fractal theory. *Ocean Dynamics*, 69(1), 59–81. <https://doi.org/10.1007/s10236-018-1229-6>
- Chmiel, O., Baselt, I., & Malcherek, A. (2018). Applicability of acoustic concentration measurements in suspensions of artificial and natural sediments using an acoustic Doppler velocimeter. *Acoustics*, 1(1), 59–77. <https://doi.org/10.3390/acoustics1010006>
- Colosimo, I., de Vet, P. L., van Maren, D. S., Reniers, A. J., Winterwerp, J. C., & van Prooijen, B. C. (2020). The impact of wind on flow and sediment transport over intertidal flats. *Journal of Marine Science and Engineering*, 8(11), 1–26. <https://doi.org/10.3390/jmse8110910>
- Conner, C. S., & De Visser, A. M. (1992). A laboratory investigation of particle size effects on an optical backscatterance sensor. *Marine Geology*, 108(2), 151–159. [https://doi.org/10.1016/0025-3227\(92\)90169-1](https://doi.org/10.1016/0025-3227(92)90169-1)
- Dankers, P. J., & Winterwerp, J. C. (2007). Hindered settling of mud flocs: Theory and validation. *Continental Shelf Research*, 27(14), 1893–1907. <https://doi.org/10.1016/j.csr.2007.03.005>
- Delft University of Technology, Utrecht University, & University of Twente. (2019). *SEAWAD: SEDiment supply At the Wadden Sea ebb-tidal Delta*. 4TU.Centre for Research Data. <https://doi.org/10.4121/collection:seawad>
- de Vet, P. L., van Prooijen, B. C., Colosimo, I., Steiner, N., Ysebaert, T., Herman, P. M., & Wang, Z. B. (2020). Variations in storm-induced bed level dynamics across intertidal flats. *Scientific Reports*, 10(1), 1–15. <https://doi.org/10.1038/s41598-020-69444-7>
- de Wit, F., Tissier, M., & Reniers, A. J. (2019). Characterizing wave shape evolution on an ebb-tidal shoal. *Journal of Marine Science and Engineering*, 7(10), 1–20. <https://doi.org/10.3390/jmse7100367>
- Downing, J. (2006). Twenty-five years with OBS sensors: The good, the bad, and the ugly. *Continental Shelf Research*, 26(17–18), 2299–2318. <https://doi.org/10.1016/j.csr.2006.07.018>
- Downing, J. P., Sternberg, R. W., & Lister, C. R. (1981). New instrumentation for the investigation of sediment suspension processes in the shallow marine environment. *Developments in Sedimentology*, 32(C), 19–34. [https://doi.org/10.1016/S0070-4571\(08\)70292-9](https://doi.org/10.1016/S0070-4571(08)70292-9)
- Eisma, D. (1993). *Suspended matter in the aquatic environment*. New York: Springer.
- Elias, E. P., Van Der Spek, A. J. F., Pearson, S. G., & Cleveringa, J. (2019). Understanding sediment bypassing processes through analysis of high-frequency observations of Ameland Inlet, the Netherlands. *Marine Geology*, 415, 10596. <https://doi.org/10.1016/j.margeo.2019.06.001>
- Fettweis, M., Riethmüller, R., Verney, R., Becker, M., Backers, J., Baeye, M., et al. (2019). Uncertainties associated with in situ high-frequency long-term observations of suspended particulate matter concentration using optical and acoustic sensors. *Progress in Oceanography*, 178, 102162. <https://doi.org/10.1016/j.pocan.2019.102162>
- Fettweis, M., Sas, M., & Monbaliu, J. (1998). Seasonal, neap–spring and tidal variation of cohesive sediment concentration in the Scheldt Estuary, Belgium. *Estuarine, Coastal and Shelf Science*, 47(1), 21–36. <https://doi.org/10.1006/ecs.1998.0338>
- Flemming, B. W., & Ziegler, K. (1995). High-resolution grain size distribution patterns and textural trends in the backbarrier environment of Spiekeroog Island (Southern North Sea). *Senckenbergiana Maritima*, 26, 1–24.
- Flores, R. P., Rijnsburger, S., Horner-Devine, A. R., Souza, A. J., & Pietrzak, J. D. (2017). The impact of storms and stratification on sediment transport in the Rhine region of freshwater influence. *Journal of Geophysical Research: Oceans*, 122, 4456–4477. <https://doi.org/10.1002/2016JC012362>
- Flores, R. P., Rijnsburger, S., Meirelles, S., Horner-Devine, A. R., Souza, A. J., Pietrzak, J. D., et al. (2018). Wave generation of gravity-driven sediment flows on a predominantly sandy seabed. *Geophysical Research Letters*, 45, 7634–7645. <https://doi.org/10.1029/2018GL077936>
- Fugate, D. C., & Friedrichs, C. T. (2002). Determining concentration and fall velocity of estuarine particle populations using ADV, OBS and LISST. *Continental Shelf Research*, 22(11–13), 1867–1886. [https://doi.org/10.1016/S0278-4343\(02\)00043-2](https://doi.org/10.1016/S0278-4343(02)00043-2)
- Gray, J., & Elliott, M. (2009). *Ecology of marine sediments* (2nd ed., 241 pp.). Oxford: Oxford University Press.
- Gray, J. R., & Gartner, J. W. (2009). Technological advances in suspended-sediment surrogate monitoring. *Water Resources Research*, 46, W00D29. <https://doi.org/10.1029/2008WR007063>
- Green, M. O., Bell, R. G., Dolphin, T. J., & Swales, A. (2000). Silt and sand transport in a deep tidal channel of a large estuary (Manukau Harbour, New Zealand). *Marine Geology*, 163(1–4), 217–240. [https://doi.org/10.1016/S0025-3227\(99\)00102-4](https://doi.org/10.1016/S0025-3227(99)00102-4)
- Green, M. O., & Boon, J. D. (1993). The measurement of constituent concentrations in nonhomogeneous sediment suspensions using optical backscatter sensors. *Marine Geology*, 110(1–2), 73–81. [https://doi.org/10.1016/0025-3227\(93\)90106-6](https://doi.org/10.1016/0025-3227(93)90106-6)
- Guo, C., He, Q., van Prooijen, B. C., Guo, L., Manning, A. J., & Bass, S. (2018). Investigation of flocculation dynamics under changing hydrodynamic forcing on an intertidal mudflat. *Marine Geology*, 395, 120–132. <https://doi.org/10.1016/j.margeo.2017.10.001>
- Ha, H. K., Hsu, W. Y., Maa, J. P., Shao, Y. Y., & Holland, C. W. (2009). Using ADV backscatter strength for measuring suspended cohesive sediment concentration. *Continental Shelf Research*, 29(10), 1310–1316. <https://doi.org/10.1016/j.csr.2009.03.001>
- Hanley, M. E., Hoggart, S. P., Simmonds, D. J., Bichot, A., Colangelo, M. A., Bozzeda, F., et al. (2014). Shifting sands? Coastal protection by sand banks, beaches and dunes. *Coastal Engineering*, 87, 136–146. <https://doi.org/10.1016/j.coastaleng.2013.10.020>
- Hawley, N. (2004). A comparison of suspended sediment concentrations measured by acoustic and optical sensors. *Journal of Great Lakes Research*, 30(2), 301–309. [https://doi.org/10.1016/S0380-1330\(04\)70348-2](https://doi.org/10.1016/S0380-1330(04)70348-2)
- Hendriks, H. C. M., van Prooijen, B. C., Aarninkhof, S. G., & Winterwerp, J. C. (2020). How human activities affect the fine sediment distribution in the Dutch Coastal Zone seabed. *Geomorphology*, 367(107), 314. <https://doi.org/10.1016/j.geomorph.2020.107314>
- Hill, D. C., Jones, S. E., & Prandle, D. (2003). Derivation of sediment resuspension rates from acoustic backscatter time-series in tidal waters. *Continental Shelf Research*, 23(1), 19–40. [https://doi.org/10.1016/S0278-4343\(02\)00170-X](https://doi.org/10.1016/S0278-4343(02)00170-X)

- Hill, P. S., Boss, E., Newgard, J. P., Law, B. A., & Milligan, T. G. (2011). Observations of the sensitivity of beam attenuation to particle size in a coastal bottom boundary layer. *Journal of Geophysical Research*, *116*, C02023. <https://doi.org/10.1029/2010JC006539>
- Hill, P. S., Milligan, T. G., & Geyer, W. R. (2000). Controls on effective settling velocity of suspended sediment in the Eel River flood plume. *Continental Shelf Research*, *20*(16), 2095–2111. [https://doi.org/10.1016/S0278-4343\(00\)00064-9](https://doi.org/10.1016/S0278-4343(00)00064-9)
- Hoitink, A. J., & Hoekstra, P. (2005). Observations of suspended sediment from ADCP and OBS measurements in a mud-dominated environment. *Coastal Engineering*, *52*(2), 103–118. <https://doi.org/10.1016/j.coastaleng.2004.09.005>
- Holland, K. T., & Elmore, P. A. (2008). A review of heterogeneous sediments in coastal environments. *Earth-Science Reviews*, *89*(3–4), 116–134. <https://doi.org/10.1016/j.earscirev.2008.03.003>
- Khelifa, A., & Hill, P. S. (2006). Models for effective density and settling velocity of flocs. *Journal of Hydraulic Research*, *44*(3), 390–401. <https://doi.org/10.1080/00221686.2006.9521690>
- Kineke, G., & Sternberg, R. (1992). Using the optical backscatterance sensor. *Marine Geology*, *108*, 253–258. [https://doi.org/10.1016/0025-3227\(92\)90199-r](https://doi.org/10.1016/0025-3227(92)90199-r)
- Lavelle, J. W., Mofjeld, H. O., & Baker, E. T. (1984). An in situ erosion rate for a fine-grained marine sediment. *Journal of Geophysical Research*, *89*(C4), 6543–6552. <https://doi.org/10.1029/JC089iC04p06543>
- Lenstra, K. J., Pluis, S. R., Ridderinkhof, W., Ruessink, G., & Van Der Vegt, M. (2019). Cyclic channel-shoal dynamics at the Ameland inlet: The impact on waves, tides, and sediment transport. *Ocean Dynamics*, *69*(4), 409–425. <https://doi.org/10.1007/s10236-019-01249-3>
- Li, Y., Jia, J., Zhu, Q., Cheng, P., Gao, S., & Wang, Y. P. (2018). Differentiating the effects of advection and resuspension on suspended sediment concentrations in a turbid estuary. *Marine Geology*, *403*, 179–190. <https://doi.org/10.1016/j.margeo.2018.06.001>
- Lin, J., He, Q., Guo, L., van Prooijen, B. C., & Wang, Z. B. (2020). An integrated optic and acoustic (IOA) approach for measuring suspended sediment concentration in highly turbid environments. *Marine Geology*, *421*(October 2019), 106062. <https://doi.org/10.1016/j.margeo.2019.106062>
- Lodder, Q. J., Wang, Z. B., Elias, E. P., Van Der Spek, A. J., de Looft, H., & Townend, I. H. (2019). Future response of the Wadden Sea tidal basins to relative sea-level rise—An aggregated modeling approach. *Water*, *11*(10), 2198. <https://doi.org/10.3390/w1102198>
- Lunven, M., & Gentien, P. (2000). Suspended sediments in a macrotidal estuary: Comparison and use of different sensors. *Oceanologica Acta*, *23*(3), 245–260. [https://doi.org/10.1016/S0399-1784\(00\)00126-2](https://doi.org/10.1016/S0399-1784(00)00126-2)
- Manning, A. J., Bass, S. J., & Dyer, K. R. (2006). Floc properties in the turbidity maximum of a mesotidal estuary during neap and spring tidal conditions. *Marine Geology*, *235*(1–4 SPEC. ISS.), 193–211. <https://doi.org/10.1016/j.margeo.2006.10.014>
- Many, G., Durrieu de Madron, X., Verney, R., Bourrin, F., Renosh, P. R., Jourdin, F., & Gangloff, A. (2019). Geometry, fractal dimension and settling velocity of flocs during flooding conditions in the Rhône ROFI. *Estuarine, Coastal and Shelf Science*, *219*, 1–13. <https://doi.org/10.1016/j.ecss.2019.01.017>
- McCave, I. N. (1984). Erosion, transport and deposition of fine-grained marine sediments. *Geological Society, London, Special Publications*, *15*(1), 35–69. <https://doi.org/10.1144/GSL.SP.1984.015.01.03>
- Mikkelsen, O. A., & Pejrup, M. (2001). The use of a LISST-100 laser particle sizer for in-situ estimates of floc size, density and settling velocity. *Geo-Marine Letters*, *20*(4), 187–195. <https://doi.org/10.1007/s003670100064>
- Milligan, T. G., & Hill, P. S. (1998). A laboratory assessment of the relative importance of turbulence, particle composition, and concentration in limiting maximal floc size and settling behavior. *Journal of Sea Research*, *39*(3–4), 227–241. [https://doi.org/10.1016/S1385-1101\(97\)00062-2](https://doi.org/10.1016/S1385-1101(97)00062-2)
- Moate, B. D., & Thorne, P. D. (2009). Measurements and inversion of acoustic scattering from suspensions having broad size distributions. *Journal of the Acoustical Society of America*, *126*(6), 2905–2917. <https://doi.org/10.1121/1.3242374>
- Moate, B. D., & Thorne, P. D. (2012). Interpreting acoustic backscatter from suspended sediments of different and mixed mineralogical composition. *Continental Shelf Research*, *46*, 67–82. <https://doi.org/10.1016/j.csr.2011.10.007>
- Moura, M. G., Quaresma, V. S., Bastos, A. C., & Veronez, P. (2011). Field observations of SPM using ADV, ADP, and OBS in a shallow estuarine system with low SPM concentration—Vitória Bay, SE Brazil. *Ocean Dynamics*, *61*(2–3), 273–283. <https://doi.org/10.1007/s10236-010-0364-5>
- Mulder, J. P. M., Hommes, S., & Horstman, E. M. (2011). Ocean & Coastal Management Implementation of coastal erosion management in the Netherlands. *Ocean & Coastal Management*, *54*(12), 888–897. <https://doi.org/10.1016/j.ocecoaman.2011.06.009>
- Nortek AS. (2005). *Vector current meter—User manual* (Tech. Rep. N 300-10 Rev. H). Vangkroken, Norway: Nortek Group.
- Nortek AS. (2008). *Aquadopp high resolution—User manual* (Tech. Rep. AHR00-0101-0508). Vangkroken, Norway: Nortek AS.
- Öztürk, M. (2017). Sediment size effects in acoustic Doppler velocimeter-derived estimates of suspended sediment concentration. *Water (Switzerland)*, *9*(7), 529. <https://doi.org/10.3390/w9070529>
- Paphitis, D., & Collins, M. B. (2005). Sand grain threshold, in relation to bed 'stress history': An experimental study. *Sedimentology*, *52*(4), 827–838. <https://doi.org/10.1111/j.1365-3091.2005.00710.x>
- Pearson, S. G., Prooijen, B. C., Elias, E. P. L., Vitousek, S., & Wang, Z. B. (2020). Sediment connectivity: A framework for analyzing coastal sediment transport pathways. *Journal of Geophysical Research: Earth Surface*, *125*, e2020JF005595. <https://doi.org/10.1029/2020JF005595>
- Pearson, S. G., van Prooijen, B., de Wit, F., Meijer-Holzhauser, H., de Looft, A., & Wang, Z. B. (2019). Observations of suspended particle size distribution on an energetic ebb-tidal delta. *Coastal sediments 2019* (pp. 1991–2003). St. Petersburg, Florida: World Scientific. https://doi.org/10.1142/9789811204487_0172
- Pomázi, F., & Baranya, S. (2020). Comparative assessment of fluvial suspended sediment concentration analysis methods. *Water*, *12*(3), 873. <https://doi.org/10.3390/w12030873>
- Pomeroy, A. W., Storlazzi, C. D., Rosenberger, K. J., Lowe, R. J., Hansen, J. E., & Buckley, M. L. (2021). The contribution of currents, sea-swell waves, and infragravity waves to suspended-sediment transport across a coral reef-lagoon system. *Journal of Geophysical Research: Oceans*, *126*, e2020JC017010. <https://doi.org/10.1029/2020JC017010>
- Postma, H. (1961). Suspended matter and Secchi disc visibility in coastal waters. *Netherlands Journal of Sea Research*, *1*(3), 359–390. [https://doi.org/10.1016/0077-7579\(61\)90009-6](https://doi.org/10.1016/0077-7579(61)90009-6)
- Reniers, A. J., de Wit, F. P., Tissier, M. F. S., Pearson, S. G., Brakenhoff, L. B., Van Der Vegt, M., et al. (2019). Wave-skewness and current-related ebb-tidal sediment transport: Observations and modeling. In *Coastal sediments 2019* (pp. 2018–2028). St. Petersburg, Florida: World Scientific. https://doi.org/10.1142/9789811204487_0174
- Rijkswaterstaat. (1999). *Sedimentatlas Waddenzee* (pp. 36–38). Haren, The Netherlands: Rijkswaterstaat.
- Roelvink, D., & Reniers, A. J. (2012). *A guide to modeling coastal morphology*. Singapore: World Scientific. <https://doi.org/10.1142/9789814304269>
- Salehi, M., & Strom, K. (2011). Using velocimeter signal to noise ratio as a surrogate measure of suspended mud concentration. *Continental Shelf Research*, *31*(9), 1020–1032. <https://doi.org/10.1016/j.csr.2011.03.008>

- Seapoint Sensors Incorporated. (2013). *Seapoint turbidity meter user manual* (Tech. Rep.). Exeter, NH: Seapoint Sensors, Inc.
- Son, C. S., Flemming, B. W., & Bartholomä, A. (2011). Evidence for sediment recirculation on an ebb-tidal delta of the East Frisian barrier-island system, southern North Sea. *Geo-Marine Letters*, *31*(2), 87–100. <https://doi.org/10.1007/s00367-010-0217-8>
- Soulsby, R. L. (1997). *Dynamics of marine sands: A manual for practical applications*. London: Thomas Telford.
- Su, M., Yao, P., Wang, Z. B., Zhang, C., Chen, Y., & Stive, M. J. (2016). Conversion of electro-optical signals to sediment concentration in a silt–sand suspension environment. *Coastal Engineering*, *114*, 284–294. <https://doi.org/10.1016/j.coastaleng.2016.04.014>
- Sutherland, T. F., Lane, P. M., Amos, C. L., & Downing, J. (2000). The calibration of optical backscatter sensors for suspended sediment of varying darkness levels. *Marine Geology*, *162*(2–4), 587–597. [https://doi.org/10.1016/S0025-3227\(99\)00080-8](https://doi.org/10.1016/S0025-3227(99)00080-8)
- Thorne, P. D., & Hanes, D. M. (2002). A review of acoustic measurement of small-scale sediment processes. *Continental Shelf Research*, *22*(4), 603–632. [https://doi.org/10.1016/S0278-4343\(01\)00101-7](https://doi.org/10.1016/S0278-4343(01)00101-7)
- Thorne, P. D., Hardcastle, P. J., & Soulsby, R. L. (1993). Analysis of acoustic measurements of suspended sediments. *Journal of Geophysical Research*, *98*(92), 899–910. <https://doi.org/10.1029/92JC01855>
- Thorne, P. D., & Hurther, D. (2014). An overview on the use of backscattered sound for measuring suspended particle size and concentration profiles in non-cohesive inorganic sediment transport studies. *Continental Shelf Research*, *73*, 97–118. <https://doi.org/10.1016/j.csr.2013.10.017>
- Thorne, P. D., Lichtman, I. D., & Hurther, D. (2021). Acoustic scattering characteristics and inversions for suspended concentration and particle size above mixed sand and mud beds. *Continental Shelf Research*, *214*, 104320. <https://doi.org/10.1016/j.csr.2020.104320>
- Thorne, P. D., & Meral, R. (2008). Formulations for the scattering properties of suspended sandy sediments for use in the application of acoustics to sediment transport processes. *Continental Shelf Research*, *28*(2), 309–317. <https://doi.org/10.1016/j.csr.2007.08.002>
- van de Kreeke, J., & Hibma, A. (2005). Observations on silt and sand transport in the throat section of the Frisian Inlet. *Coastal Engineering*, *52*(2), 159–175. <https://doi.org/10.1016/j.coastaleng.2004.10.002>
- Van Der Hout, C. M., Witbaard, R., Bergman, M. J. N., Duineveld, G. C. A., Rozemeijer, M. J. C., & Gerkema, T. (2017). The dynamics of suspended particulate matter (SPM) and chlorophyll-*a* from intratidal to annual time scales in a coastal turbidity maximum. *Journal of Sea Research*, *127*, 105–118. <https://doi.org/10.1016/j.seares.2017.04.011>
- Van Der Werf, J., Antolínez, J. A. Á., Brakenhoff, L., Gawehn, M., den Heijer, K., de Looft, H., et al. (2019). *Datareport Kustgenese 2.0* (Tech. Rep. 1220339-015-ZKS-0004). Delft, The Netherlands: Rijkswaterstaat.
- van Prooijen, B. C., Tissier, M. F., de Wit, F. P., Pearson, S. G., Brakenhoff, L. B., van Maarseveen, M. C., et al. (2020). Measurements of hydrodynamics, sediment, morphology and benthos on Ameland ebb-tidal delta and lower shoreface. *Earth System Science Data*, *12*(4), 2775–2786. <https://doi.org/10.5194/essd-12-2775-2020>
- Voulgaris, G., & Meyers, S. T. (2004). Temporal variability of hydrodynamics, sediment concentration and sediment settling velocity in a tidal creek. *Continental Shelf Research*, *24*(15), 1659–1683. <https://doi.org/10.1016/j.csr.2004.05.006>
- Wang, Z. B., Elias, E. P., Van Der Spek, A. J., & Lodder, Q. J. (2018). Sediment budget and morphological development of the Dutch Wadden Sea: Impact of accelerated sea-level rise and subsidence until 2100. *Netherlands Journal of Geosciences*, *97*(3), 183–214. <https://doi.org/10.1017/njg.2018.8>
- Weeks, A. R., Simpson, J. H., & Bowers, D. (1993). The relationship between concentrations of suspended particulate material and tidal processes in the Irish Sea. *Continental Shelf Research*, *13*(12), 1325–1334. [https://doi.org/10.1016/0278-4343\(93\)90086-D](https://doi.org/10.1016/0278-4343(93)90086-D)
- WETLabs. (2010). *ECO 3-measurement sensor user's guide* (Tech. Rep.). Philomath, OR: WET Labs, Inc.
- WET Labs Inc. (2019). *User manual: ECO fluorometers and scattering sensors* (Tech. Rep.). Philomath, OR: WET Labs Inc.
- White, T. E. (1998). Status of measurement techniques for coastal sediment transport. *Coastal Engineering*, *35*(1–2), 17–45. [https://doi.org/10.1016/S0378-3839\(98\)00033-7](https://doi.org/10.1016/S0378-3839(98)00033-7)
- Wilson, G. W., & Hay, A. E. (2015). Measuring multi-phase particle flux with a multi-frequency acoustic profiler. *Proceedings of the Institute of Acoustics*, *37*, 343–3819. <https://doi.org/10.1121/1.4938219>
- Winkelmolen, A. M., & Veenstra, H. J. (1974). Size and shape sorting in a Dutch tidal inlet. *Sedimentology*, *21*(1), 107–126. <https://doi.org/10.1111/j.1365-3091.1974.tb01784.x>
- YSI Incorporated. (2012). *6-Series multiparameter water quality Sondes user manual* (revision j ed., 374 pp.). Yellow Springs, OH: YSI Incorporated.
- Zhu, Q., van Prooijen, B. C., Maan, D. C., Wang, Z. B., Yao, P., Daggars, T., & Yang, S. L. (2019). The heterogeneity of mudflat erodibility. *Geomorphology*, *345*, 106834. <https://doi.org/10.1016/j.geomorph.2019.106834>

Reference From the Supporting Information

- Aminot, A., & Kérouel, R. (2004). *Hydrologie des écosystèmes marins: Paramètres et analyses* (1 ed., 336 pp.). IFREMER.